MODELING OF TIME-DEPENDENT ELECTRON IMPACT SOURCE FUNCTIONS IN INDUCTIVELY COUPLED PLASMAS USING AN “ON-THE-FLY” MONTE-CARLO TECHNIQUE

BY

ARVIND SANKARAN

B.Tech., Indian Institute of Technology, Madras, 1999

THESIS
Submitted in partial fulfillment of the requirements
for the degree of Master of Science in Chemical Engineering
in the Graduate College of the
University of Illinois at Urbana-Champaign, 2001

Urbana, Illinois

(RED BORDERED SIGNATURE PAGE HERE)

MODELING OF TIME-DEPENDENT ELECTRON IMPACT SOURCE FUCNTIONS IN INDUCTIVELY COUPLED PLASMAS USING AN "ON-THE-FLY" MONTE-CARLO TECHNIQUE

Arvind Sankaran, M.S.
Department of Chemical Engineering
University of Illinois at Urbana-Champaign, 2001
Mark J. Kushner, Advisor

Electron temperatures in low-pressure inductively coupled plasma reactors do not significantly vary during the rf cycle. There can be, however, considerable modulation of the rate coefficients and the source functions of electron impact reactions having high threshold energies. This results from the electron energy distribution being less collisional at higher energies. In many instances, it is convenient to use cycle-averaged values for these quantities due to the computational burden in computing and storing space and time-dependent electron energy distributions. In this thesis a new "On-the-Fly" Monte-Carlo technique is described to address these time-dependent plasma parameters. The On-the-Fly Monte-Carlo method, unlike conventional methods, stores only the moments of the electron energy distributions and not the distributions themselves. This method reduces the computational complexities and is useful in extending this model to calculate the harmonic components.

The On-the-Fly technique was incorporated in the two-dimensional Hybrid Plasma Equipment Model to investigate the time-dependence of electron impact source functions. The consequences of varying the rf electric field frequency, gas pressures, rf magnetic field, and composition of the gas mixture on the harmonic content of the source functions are quantified. Even harmonics were more dominant than the odd harmonics. The harmonic content decreased with increasing frequencies and it increased with increasing pressure. The harmonic content of

the source functions was more pronounced when N_2 content was increased in Ar/N_2 gas mixtures.

ACKNOWLEDGMENTS

I would like to express my sincere gratitude to my advisor, Prof. Mark J. Kushner, whose help and guidance have been the scaffold of this work. I am profoundly thankful to him for being patient with me and helping me solve all the difficulties in my work and otherwise. All my knowledge and understanding in plasma physics, I attribute to him.

I would like to acknowledge the support of the Semiconductor Research Corporation (SRC), National Science Foundation (NSF) and Defense Advanced Research Projects Agency (DARPA).

I take this opportunity to thank all fellow members in the Computational Optical and Discharge Physics Group: Ron Kinder, Da Zhang, Junquing Lu, Dan Cronin, Rajesh Dorai, Pramod Subramonium, Brian Lay, Kapil Rajaraman, Vivek Vyas, Sang-Hoon Cho, Gary Eden and Kelly Collier. Special thanks to Rajesh for sharing not only the office space but also all the hurdles that I faced in my work.

My aunt Bhavani and my parents, Savithri and Sankaran, have showed endless love and encouragement throughout my career, without which I would not be the person I am. My sister and friend Aparna has shared all my problems and has always helped me with timely advice and constructive criticism, and my grandmother's faith in me has always motivated me. My aunt Meena and her family have always supported me in all my endeavors. I thank them all for all their help and support, which have helped in shaping my dreams and efforts into this work. This note would be incomplete if I didn't thank all my other friends and relatives for their support.

TABLE OF CONTENTS

1. INTRODUCTION

1.1 Development of Plasma Processing Tools

Plasma processing is an important technology for an increasing number of industries, including semiconductor manufacturing, medical products, and environmental pollution control.[1] Due to the increasing cost and time required to develop these complex apparatuses, computer modeling is becoming more prevalent in the design cycle. The development of plasma equipment models for investigating and understanding complex plasma processes has significantly advanced over the last few years. New algorithms and modeling techniques are being developed to address both more fundamental and more industrially interesting problems. Successful use of models for processes like plasma etching critically depends on the validity of the models. Due to these stringent requirements, plasma equipment models must minimize on the underlying assumptions that go into their development and use the most fundamental approach possible.

Traditionally plasma equipment models for low-pressure, partially coupled systems have used values averaged over radio frequency (rf) cycle in determining the rate coefficients and the source functions of electron impact reactions. Although it has been noted that electron temperatures in low-pressure inductively coupled plasmas do not significantly vary during the rf cycle, the rate coefficients and the source functions of electron impact reactions do have significant time dependence during the rf cycle due to the complex behavior of the electron energy distribution function. As a result, incorporation of the time dependence of such plasma parameters into plasma equipment models is an important consideration. In particular, including

time harmonics of the sources will better represent these rates and can hence give a more accurate representation of the plasma parameters.

1.2 Models Using Time Dependent Rates

Most of the earlier work done in this field addressing time-dependent rates has been on rf capacitively coupled discharges. Most models assume the discharge electrodes to be parallel plates with sufficiently large diameters compared to their separation so that the system can be approximated as depending only on axial position between electrodes. All of the work shown below has incorporated and shown significant time dependence of the excitation rates and electron and ion densities.

Bletzinger and DeJoseph[2] examined optical emission from 13.56 MHz rf discharges in nitrogen and obtained the corresponding electron impact excitation rate profiles. The key features that they have observed are that the peak in excitation rate occurs around the cathodic phase of the rf period for each electrode and the peak intensity increases when moving away from the local electrode. Flamm and Donnely[3] measured electron impact excitation rate profiles in chlorine discharges and found that at 13.2 MHz emission peaked near the positive electrode. This suggests that electrons accelerate toward the electrode around the anodic part of the cycle, indicating significant time dependence.

Graves[4] developed a hybrid rf discharge model that solves for the ion continuity equation, electron energy balance equation, Poisson's equation, and the electron and ion momentum balance equations simultaneously to obtain the plasma processing parameters. Solutions thus obtained were expanded in a Fourier series in time and linear finite element basis functions in space. The use of Fourier series to represent the time dependence of the solution forces time

periodicity. The solutions in the Fourier domain in this case are symmetric. The coefficients of odd harmonics are zero at the midplane of the discharge, and gradients of coefficients of even harmonics are zero at the midplane. In this simulation 35 finite elements in space and 13 Fourier coefficients were used. The voltage applied in this case is referred to as the push-pull mode, wherein the voltage is applied symmetrically to both electrodes. As the voltage increases at one electrode, it decreases at the other. The ion density remained almost a constant within a rf cycle, while there was significant modulation of the electron density, current density, Joule heating, temperature, and excitation rates. The time dimension was represented as a fraction of the rf cycle, and 0.75 corresponds to maximum negative voltage at the electrode. A peak was observed which originates near the local electrode around time 0.6 and increases in magnitude as it moves away from the electrode. It then attenuates and broadens as it merges with the plasma "continuum" excitation in the center of the discharge. The same emission pattern is observed near the other electrode. The peak at 0.6 is explained on the basis of the time dependence of the Joule heating and the temperature profile in the discharge cell. These results were also compared with experimental results and a close match was obtained.

Sommerer *et al.*[5] investigated a similar system with a discharge gap of 4 cm between the electrodes. A 0.1 Torr helium discharge system operating at a frequency of 13.56 MHz was used. A sinusoidal voltage of 500 V was applied. Results for this benchmark case showed an ion density constant over a cycle while the total current to each electrode was significantly varying over the cycle. The important result noted by the authors revealed that the bulk electric field was largely out of phase with the sheath electric field. The ionization rate peaked near the sheath-bulk boundary because during the cathodic phase the expanding sheath accelerates the electrons that have migrated toward the electrode during the anodic cycle. In this system, the

low-energy bulk electrons respond to the bulk field, but require on the order of an rf cycle to cross the bulk, whereas the high energy electrons can cross the bulk several times per rf cycle. Because the high-energy electrons can have twice the mean free path, they can cross the bulk and collide with the sheath at any time. Thus the high-energy electrons increase the total ionization during the first tracking cycle by 20% whereas the low energy electrons halves the total ionization.

Meyyappan *et al.*[6-8] studied similar systems. The authors considered a symmetric, capacitively coupled, parallel plate electrode and simplified it to a 1-D system. The hybrid model they developed was applied to electropositive discharges. Ar/molecular gas discharges were considered. The time dependence of the excitation rates and the ionization rates were established and compared with the time-averaged values. The ionization rate peaked between time 0.25 and 0.75 and this position varied with time. The velocity of this shift in the maximum is computed to be about 5×10^{7} cm-s^{-1}. Surendra *et al.*[9] referred to this phenomenon as a moving pulse.

1.3 Conclusions

From these examples, the importance of the time dependence of the excitation rates and the source functions of electron impact reactions is clear. Most of the work on time-dependent excitation to date has used 1-D models and so does not include spatial variations in two dimensions. In this work the variation of rates and source functions are studied both spatially in 2-D and in time for inductively coupled plasma reactors. The time variation of the source functions so determined is also used to update the source functions and to obtain a more realistic representation of plasma parameters.

The algorithms developed in this work were incorporated into the 2-D Hybrid Plasma Equipment Model (HPEM) which is explained in detail in Chapter 2. As an introduction, the HPEM consists of three modules: the Electromagnetics Module (EMM), Electron Energy Transport Module (EETM), and Fluid Kinetics Simulation (FKS). The modules are executed iteratively until convergence. The rates and the source functions of electron impact reactions are calculated in the EETM module using Monte Carlo techniques. Investigation of the time dependence of the rates involves calculating of the corresponding Fourier components in time (harmonics) which requires obtaining the electron energy distribution functions (EED) both spatially and temporally. The conventional technique requires the explicit calculation and storing of the EEDs, which requires more computer memory. This increases the computational complexity, and due to binning less accurate solutions are obtained. To this end, a new "On-the-Fly" technique has been proposed and developed, wherein only the moments of the distribution functions are calculated as opposed to the distribution functions themselves. The On-the-Fly technique and its extension to the study of harmonic components of source functions are explained in Chapter 2 as well.

This model is then used to investigate Ar/N_2 gas mixtures in an ICP reactor and the results of the simulations are presented in Chapter 3. The process parameters are studied for low-pressure systems. The variation of the harmonic content of source functions of electron impact reactions are quantitatively analyzed as a function of the threshold energy of the reactions, pressure, frequency, and rf magnetic fields. The consequences of gas mixtures are also obtained. Finally, conclusions are presented in Chapter 4.

1.4 References

[1] J. R. Roth, Industrial Plasma Engineering, Volume 1. (1995)

[2] P. Bletzinger and C.A. DeJoseph, Jr., IEEE Trans. Plasma Sci. **PS-14,** 124 (1986)

[3] D. L. Flamm and V. M. Donnelly, J. Appl. Phys. **59**, 1052 (1986)

[4] D. B. Graves, J. Appl. Phys. **62**, 88 (1987)

[5] T. J. Sommerer, W. N. G. Hitchon, and J. E. Lawler, Phys. Rev. Lett. **63**, 2361 (1989)

[6] M. Meyyappan and T. R. Govindan, IEEE Trans. Plasma Sci. **PS-19**, 122 (1991)

[7] M. Meyyappan, J. Appl. Phys. **69**, 8047 (1991)

[8] M. Meyyappan and T. R. Govindan, J. Appl. Phys. **74**, 2250 (1993)

[9] M. Surendra, D. B. Graves, and I. J. Morey, Appl. Phys. Rev. Lett. **56**, 1022 (1990)

2. DESCRIPTION OF THE MODEL

2.1. Introduction

In this chapter, the models and the techniques used for these investigations are described. All the algorithms developed in this work have been integrated in the Hybrid Plasma Equipment Model (HPEM). An overview of the HPEM is given here so that the thesis work can be understood in the context of the entire hierarchy. The new Monte Carlo On-the-Fly technique in HPEM will be described. The On-the-Fly technique is validated, and its extension to calculate harmonic components of the source functions is also discussed in this chapter.

2.2 Hybrid Plasma Equipment Model (HPEM)

The HPEM is a plasma equipment model developed by the Computational Optical and Discharge Physics Group to numerically investigate low-pressure and low temperature plasma processing reactors in two and three dimensions [1-10]. The HPEM can model a variety of reactor geometries, and it can analyze different gas chemistries and generate the corresponding plasma parameters. The HPEM addresses the plasma physics and plasma chemistry in a modular fashion. The main modules are the Electromagnetics Module (EMM), Electron Energy Transport Module (EETM), and Fluid Kinetics Simulation (FKS). The HPEM iterates on these different coupled modules to generate the plasma parameters. The inductively coupled electromagnetic fields and magnetostatic fields are computed in the EMM, which is discussed in Section 2.3. These fields are used in the EETM to generate the electron energy distribution functions; electron temperature and electron impact rate coefficients as a function of position either by using an Electron Monte Carlo simulation (EMCS) or by solution of the fluid electron energy

equation coupled with a solution of the Boltzmann equation. This module is discussed in Section 2.4. Results of the EETM are transferred to the FKS module to determine plasma source and sink terms. The FKS solves the fluid continuity equations for species densities and plasma conductivity and solves Poisson's equation for the electrostatic fields. The densities, conductivity, and electric fields obtained from the FKS are then transferred to the EMM and EETM. These three modules are solved successively until a converged solution is obtained or until a preset number of total iterations is finished.

Several off-line modules of the HPEM have been developed for other specific purposes. The Plasma Chemistry Monte Carlo Simulation (PCMCS) computes energy and angular dependencies of fluxes at specified surface locations by using outputs from HPEM.[8] The Monte Carlo Feature Profile Model (MCFPM) uses the result of the PCMCS to simulate micro-scale feature profile.[10] The structure of these modules are described in greater detail elsewhere [1-10]. A flow diagram of the HPEM is shown in Fig. 2.1.

2.2.1 The Electromagnetics Module

The solution for the electromagnetic fields requires knowledge of the plasma conductivity, which is obtained from the other modules. The EMM provides time-harmonic azimuthal electromagnetic fields, and it provides the static magnetic fields generated by the permanent magnets or by equivalent dc loops, that is, currents that change on time scales which are long compared to the time in which the plasma reaches quasi-equilibrium.

The EMM module calculates the spatially dependent azimuthal electric fields by solving Maxwell's equation under time harmonic conditions. Assuming azimuthal symmetry, Maxwell's equation for electric fields is reduced to

$$-\nabla\cdot\frac{1}{\mu}\nabla E_f = \omega^2\varepsilon E_f - i\omega J_f\,, \tag{2.1}$$

where μ is the permeability, E_f is the azimuthal electric field, ω is the frequency of the source current, ε is the permittivity, and J_f is the total current consisting of driving and conduction currents. The conduction current J_c is calculated from $J_c = \sigma E_f$, where σ is the conductivity. At pressures where the electrons are sufficiently collisional, the conductivity of the plasma is

$$\sigma = \frac{q_e^2 n_e}{m_e}\frac{1}{\nu_{me} + i\omega}, \tag{2.2}$$

where q_e is the unit electron charge, n_e represents electron density, m_e denotes electron mass, ν_{me} is the momentum transfer collision frequency of electrons, and ω is the driving frequency. Maxwell's equations are solved using the method of successive over relaxation (SOR). The weighting coefficients and the convergence criterion for the SOR are adjustable simulation parameters.

The static magnetic fields are solved in the radial and vertical directions assuming azimuthal symmetry. Under these conditions, the magnetic field can be represented as a vector potential which has only a single component in the ϕ direction. The current loops, which provide source terms when solving for vector potential **A**, by differentiation, yields the static magnetic fields

$$\nabla \times \mathbf{A} = \mathbf{B}; \quad \nabla \times \frac{1}{m} \nabla \times \mathbf{A} = \mathbf{j}, \tag{2.3}$$

where m is the permeability, and $\mathbf{j}$ is the current density of the source current loops. The vector potential is solved as a boundary value problem using SOR, with the same convergence criteria as the electric field.

A circuit module (CM) is included in the EMM which models a matchbox circuit as well as the coils. The impedance of the matchbox is matched to the coil impedance, allowing the deposited power to be maximized. The source voltage is also adjusted from iteration, to iteration allowing the power specified by the input file to be matched and maintained.

2.2.2 The Fluid Kinetics Simulation

In the FKS, the continuum transport equations for the gas species are solved simultaneously with the electrostatic potential to determine the spatial distribution of species densities as well as the momentum flux fields within the reactor. To solve for these plasma properties, the electron transport properties and the chemical reaction rates are obtained from the EETM. Ion and neutral transport coefficients are obtained from a database or by using Lenard-Jones parameters. To self consistently consider the electrostatic fields, either Poisson's equation can be included, or quasi-neutrality allowing ambipolar fields can be assumed. The continuity equation for all species is

$$\frac{\partial N_i}{\partial t} = -\nabla \cdot \Gamma_i + S_i \tag{2.4}$$

which can be used to solve for the species densities where N_i, Γ_i, and S_i are the respective density, flux, and sources for species *i*.

The electron flux Γ_i is determined by the drift diffusion equation

$$\Gamma_i = m_i q_i N_i \overline{E}_s - D_i \nabla N_i \tag{2.5}$$

where μ_i is the mobility of species *i*, D_i is the diffusion coefficient, q_i is the species charge in units of elementary charge, and E_s is the electrostatic field. The ion and neutral flux calculation can be done using the drift diffusion equation or by including the effects of momentum by the replacement of the diffusional term with terms for pressure, advection, and collisionality

$$\frac{\partial \Gamma_i}{\partial t} = -\frac{1}{m_i}\nabla\left(N_i kT_i\right) - \nabla\cdot\left(N_i \overline{v}_i \overline{v}_i\right) + \frac{q_i}{m_i} N_i \overline{E} - \sum_j \frac{m_j}{m_i + m_j} N_i N_j \left(\overline{v}_i - \overline{v}_j\right)\nu_{ij} \tag{2.6}$$

where T_i is the species temperature, $\overline{v}_i$ is the species velocity given by Γ_i / N_i, and ν_{ij} is the collision frequency between species *i* and species *j*. The viscosity is included for neutrals only. Determination of the time-dependent electrostatic fields is accomplished either by solution of Poisson's equation or based on quasi-neutrality allowing an ambipolar approximation. Poisson's equation is given by

$$\nabla\cdot\left(\left(\varepsilon - \Delta t\,\sigma + \Delta t \sum_i q_i^{\,2} m_i N_i^{\,2}\right)\nabla \phi^{t+\Delta t}\right) = -\rho^{t} + \Delta t \nabla\cdot\left(\sum_i q_i D_i \nabla N_i^{\,t} - \sum q_j \Gamma_j^{\,t}\right) \tag{2.7}$$

where σ is the material conductivity and is nonzero only outside of the plasma region e is elemental charge; q_i, μ_i, N_i, and Γ_i are the charge state, mobility, density, and flux of species i at time t, respectively; Γ_j is the flux for species j at time t; and $\phi^{t+\Delta t}$ is the electric potential at time $t + \Delta t$. Poisson's equation is calculated semi-implicitly by approximating the charge density linearly as

$$\boldsymbol{r}^{t+\Delta t} = \boldsymbol{r}^{t} + \Delta t \cdot \left.\frac{\partial \boldsymbol{r}}{\partial t}\right|^{t+\Delta t} \tag{2.8}$$

where $\rho^{t+\Delta t}$ is the charge density at time $t+\Delta t$, and $\boldsymbol{r}^t$ is the charge density at time t. The evolution rate of the charge density $\partial\rho/\partial t$ is determined by the divergence of the total current density $\mathbf{j}$:

$$\frac{\partial \boldsymbol{r}}{\partial t} = -\nabla \cdot \mathbf{j} + S\,, \tag{2.9}$$

where S is the source function of charges. In the plasma region, $\mathbf{j} = q_i(-D_i \nabla n_i + q_i \mu_i(-\nabla f))$ for electrons and $\mathbf{j} = q\Gamma$ for ions. In materials, $\mathbf{j} = \sigma(-\nabla f)$ where σ is the material conductivity. By making the potential fully implicit in this scheme while using explicit terms for the assumedly more slowly varying species properties such as density and temperature, the time step used in the SOR solution can be lengthened beyond the dielectric relaxation time and greatly accelerate solution over the fully explicit formulation.

The second option is to compute electrostatic fields using a quasi-neutrality approximation over the entire plasma region. Under such an assumption the electron density can

be set equal to the total ion density at all locations. To maintain this charge neutrality requires that

$$-\nabla \cdot \Gamma_e + S_e = \sum_i q_i(-\nabla \cdot \Gamma_i + S_i) \tag{2.10}$$

or

$$\nabla \cdot (m_e n_e \nabla \boldsymbol{f} + D_e \nabla n_e) + S_e = \sum_i q_i(\nabla \cdot (-m_i n_i \nabla \boldsymbol{f} + D_i \nabla n_i) + S_i) \tag{2.11}$$

where S_e and S_i represent electron and ion source functions, respectively, due to both internal and external sources such as electron beams. The flux terms are replaced by their drift diffusion approximations and the terms are rearranged to get

$$\sum_i q_i \nabla \cdot (q_i n_i \mu_i \nabla \phi - D_i \nabla n_i) = \sum_i q_i S_i \tag{2.12}$$

where the summations are taken over all charged species including both electrons and ions. By reducing the system to a steady-state solution, the dielectric relaxation time is removed as a limit allowing much larger time steps to be taken, which are limited only by the Courant limit.

A semi-analytic sheath model (SM) has also been integrated with the FKS to represent the fields and fluxes at gas-solid boundaries under conditions where the actual sheath thickness is less than the mesh spacing. A multi-species form of Riley's unified sheath model[11] is used to relate the sheath charge Q and boundary conditions to the potential drop. This potential drop across the sheath produced by the semi-analytic sheath model is then applied as a jump condition at plasma wall boundaries in solving Poisson's equation for the entire reactor.

2.2.3 The Electron Energy Transport Module

In the Electron Energy Transport Module, the power deposition into the electrons, as well as the electron impact sources, is modeled and the electron transport properties are computed. These can be solved in two different ways in the HPEM. The first method is to solve the 2-D electron energy equation. Electron transport properties as a function of temperature are obtained by solving the 0-D Boltzmann equation. The second method is to run a Monte Carlo simulation, in which electron pseudo-particles are moved in the computed fields and have collisions with the other plasma species. The trajectories are integrated over a period of time and the statistics are collected to generate the electron energy distribution functions (EEDs), which are then used to calculate the rate coefficients.

2.2.3.1 The Electron Energy Equation Method

The Electron Energy Equation Method first numerically solves the 0-D Boltzmann equation for a range of values of electric field divided by total gas density (E/N) in order to create a table of values, which correlate E/N with an EED. The Boltzmann equation is expressed as

$$\frac{\partial f_e}{\partial t} + \mathbf{v}\cdot\nabla_{\mathbf{r}} f_e - \frac{e(\mathbf{E}+\mathbf{v}\times\mathbf{B})}{m_e}\cdot\nabla_{\mathbf{v}} f_e = \left(\frac{df_e}{dt}\right)_{collision}, \tag{2.13}$$

where $f_e = f_e(t, \boldsymbol{r}, \boldsymbol{v})$ is the electron distribution function, $\nabla_{\mathbf{r}}$ is the spatial gradient, $\nabla_{\mathbf{v}}$ is the velocity gradient, m_e is the electron mass, and $\left(\frac{df_e}{dt}\right)_{collision}$ represents the effect of collisions. The resulting values are then used as a lookup table, which yields electron mobility, thermal

conductivity, energy-loss rate due to collisions and electron impact rate coefficients as a function of electron temperature. T_e is defined as 3/2 $<\varepsilon>$, where $<\varepsilon>$ is the average energy computed from the EEDs.

With the EEDs known as a function of temperature, the steady state electron energy equation is solved as follows

$$\nabla \boldsymbol{k} \nabla T_e + \nabla \cdot (\Gamma_e T_e) = P_h - P_l \ , \tag{2.14}$$

where $\boldsymbol{k}$ is the thermal conductivity, T_e is the electron temperature, Γ_e is the electron flux, P_h is the electron heating due to deposition, and P_l is the power loss due to inelastic collisions. The electron flux Γ is computed in the FKS, and the power deposition rate is computed from the time-averaged value of j.E, where $\mathbf{j} = \boldsymbol{s}E - qD\nabla n_e$. The electric field is both the inductive field computed in the EMM and the capacitively coupled field computed in the FKS. The above equation is discretized and solved by SOR, with the transport coefficients updated based on the local electron temperature.

2.2.3.2 The Electron Monte Carlo Method

The Monte Carlo method is a fully kinetic treatment, which resolves the gyro motion of electrons in magnetic fields using a semi-implicit technique. Noncollisional heating is kinetically resolved by producing electron currents, which are used to correct the assumption of collisional power deposition in the EMM.

The Electron Monte Carlo Simulation (EMCS) tracks the trajectory of electron pseudo-particles by moving them in the computed electric and magnetic fields as a function of time. A

group of electrons is initialized from a Maxwellian distribution and randomly distributed within the rf period, with starting locations randomly determined within the reactor volume weighted by the electron density computed in the FKS. The electron energy range is divided into discretized energy bins for collision determination and this binning also helps in collecting statistics. The collision frequency ν_i within any energy bin is computed by summing all possible collision within the energy range

$$\boldsymbol{n}_i = \left(\frac{2\boldsymbol{e}_i}{m_e}\right)^{\frac{1}{2}} \sum_{j,k} \boldsymbol{s}_{ijk} N_j \tag{2.15}$$

where ε_i is the average energy within the bin, σ_{ijk} is the cross section at energy *i,* for species *j* and collision process *k*, and N_j is the number density of species *j*. The time between the collisions is randomly determined using the maximum collision frequency for all energy bins. $\Delta t = \frac{-1}{\boldsymbol{u}} \ln(r)$, *r*= (0,1). At the time of a collision, the reaction that occurs is chosen randomly from all the possible reactions for that energy bin. A null collision cross section makes up the difference between the actual collision frequency and the maximum collision frequency at any given spatial location. In this work electron-electron collisions are not considered. The velocity of the electrons is adjusted based on the type of collision it undergoes. If the collision is null then the electron's trajectory is unaltered. Particles are integrated using the Lorentz equation.

$$\frac{d\bar{v}}{dt} = \frac{q_e}{m_e}\left(\bar{E} + \bar{v} \times \bar{B}\right) \tag{2.16}$$

and

$$\frac{d\bar{r}}{dt} = \bar{v} \tag{2.17}$$

where $\bar{v}$, $\bar{E}$, and $\bar{B}$ are the electron velocity, local electric field, and magnetic field respectively. Eq. (2.16) and (2.17) are updated using a second-order predictor corrector scheme. Electric fields are both the inductive fields computed in the EMM and the time-dependent static fields computed in the FKS. Time steps are chosen to be less than both 1% of the rf period and 1% of the cyclotron frequency, and small enough that the particles do not cross more than one-half computational cell in one time step. Several hundred to a few thousand particles are integrated in time for many rf cycles, typically greater than 100 rf cycles.

The statistics for computing the electron energy distributions (EEDs) are updated every time an electron is moved in the mesh, which is at every time step. These statistics are collected into an array for energy i and location l.

$$F_{il} = \sum_j w_j d\left((e_i \pm 1/2\ \Delta e_i) - e_j\right) d\left((\vec{r}_l \pm \Delta\vec{r}) - \vec{r}_j\right) \tag{2.18}$$

where the summation is over particles, w_j is the weighting of the particle, ε_i is the energy and r_k is the bin location. The weighting w_j is a product of three factors; the relative number of electrons each pseudo-particle represents, the time step used to advance the trajectory, and a spatial weighting obtained using the method of finite-sized particles (FSP). At the end of the EMCS, the electron temperature, collision frequency and electron-impact rate coefficients are computed as a function of position from the EEDs. The EEDs f_{ik} are obtained from the raw statistics F_{ik} by requiring normalization of each spatial location.

$$\sum_i F_{ik}\Delta e_i = \sum_i f_{ik} e_i^{\frac{1}{2}} \Delta e_i = 1 \tag{2.19}$$

The electron temperature is defined by convention to be 2/3 <ε>. The electron impact rate coefficient (k_m) for electron impact process m and location l is computed as

$$k_{ml} = \int_0^\infty \left(\frac{2e}{m_e}\right)^{\frac{1}{2}} s_m(e) f_l(e) e^{\frac{1}{2}} de = \sum_i \left(\frac{2e_i}{m_e}\right)^{\frac{1}{2}} s_{mi} f_{il}(e) e_i^{\frac{1}{2}} \Delta e \tag{2.20}$$

$$k_{ml} = \frac{\sum_i F_{il} u_i s_{mi} \Delta e_i}{\sum_i F_{il} \Delta e_i} \tag{2.21}$$

2.3 On-the-Fly Method

This method is an improvisation on the existing Monte Carlo algorithm and is a Mont Carlo based algorithm in which only moments of the distribution function are calculated On-the-Fly. As a result, in contrast to the original Monte Carlo method, the distribution functions are not calculated explicitly and thus are not stored either. The basic algorithm for launching and moving the electrons in the mesh and for keeping track of the collisions remains the same. As before the statistics are collected at each mesh point as and when an electron is touched. But in the On-the-Fly method the intermediate step of calculating the distribution function is avoided, an instead only the moments of the distribution function is stored.

In this method the collection of raw statistics F_{il} is replaced by a continuing summation whose asymptotic value produces the k_{ml} described by Eq. (2.21). That is, at time step s, we compute

$$\begin{aligned} \Delta k_{ml}^{s} &= \sum_{j} w_j d\left((\vec{r}_l \pm \Delta\vec{r}) - \vec{r}_j\right) s_m(e_j) u_j \Delta t_j \\ \Delta w_l^{s} &= \sum_{j} w_j \Delta t_j d\left((\vec{r}_l \pm \Delta\vec{r}) - \vec{r}_j\right) \end{aligned} \tag{2.22}$$

where Δk^{s}_{ml} and Δw^{s}_{l} are the incremental update to the rate coefficient and total weighting. The rate coefficient at time s is then obtained from

$$\begin{aligned} k_{ml}^{s} &= \frac{k_{ml}^{s-1}.w_{ml}^{s-1} + \Delta k_{ml}^{s}}{w_l^{s}} \\ where\ w_l^{s} &= w_l^{s-1} + \Delta w_l^{s} \end{aligned} \tag{2.23}$$

Using this method, the rate coefficient k_{ml} is instantaneously available at any time. As time progresses and more statistics are gathered, k_{ml} simply becomes more accurate.

The On-the-Fly method has many potential advantages over the conventional MCS method. This technique is more accurate than calculating the intermediate f_i and calculating the rate coefficients from them because the OTF method avoids discretization or the binning of the electrons or ion energies, and hence can utilize the full continuum nature of the EED. Thus binning over energy is avoided and the only binning is over space. This method is advantageous from a computational standpoint as well. Since moments of the distribution function are less sensitive to statistical noise than the EED itself, fewer particles are required in the simulation. Also, since the EEDs are not explicitly calculated and hence energy binning avoided, the storage

space requirement is smaller, an important consideration in 3-D simulation. Also, since the rate coefficients and the transport properties can be calculated within the EETM module and not at the end of the module as the conventional technique, the parallelization of the HPEM code becomes more advantageous. This method can lastly be extended to include the Fourier components in time of the rate coefficients, which in case of the conventional method is cumbersome. The calculation of these harmonics is presented in the next section.

The conventional MCS method and the On-the-Fly technique were compared for an ICP reactor using Ar/N_2 gas mixtures. The gas pressure was 5 mTorr. The frequency of the rf electric field was 13.56 MHz. Neutral gas temperature in the cell was about 400 K. The power deposition was 650 W and the gas mixture was Ar/N_2 = 90/10. Comparison of both the methods was based on their electron density profiles and source function profiles. The electron density profile for both the methods is presented in Fig. 2.2. The electron density obtained using the conventional method has a high value of 3.2×10^{11} cm^{-3} and a low value of 2.1×10^{11} cm^{-3} near the gas outlet. In case of the OTF method electron density has a high value of 3.4×10^{11} cm^{-3} and a low value of 2.2×10^{11} cm^{-3} near the gas outlet. Both the methods show similarity in terms of the high and low values of their electron density profiles. Even the spatial variation of the electron density shows exactly the same trend in both methods, indicating the similarity of both the methods.

The source function of electron impact ionization of Ar obtained using both methods is presented in Fig. 2.3. The spatial variations of the source functions in both the methods are similar. This shows a close match between both the models and thus confirms the accuracy of the OTF method.

2.4 Extension of the On-the-Fly Method to Calculate Harmonics

One of the advantages of the On-the-Fly technique over the conventional Monte Carlo methods is its ability to be extended to calculate the Fourier components of the transport coefficients and hence the source functions of the electron impact reactions as well. This ultimately enables one to include time dependent source functions in the FKS, as opposed to time-averaged. The study of the harmonic components as described earlier is significant and gives a more accurate representation of the plasma parameters.

To calculate the Fourier components of the electron impact source functions the corresponding frequency terms are incorporated into Eq. (2.22). For example the Fourier component for the n^{th} harmonic at frequency $n\omega$ is obtained from replacing Eq. (2.22) with

$$\Delta k^{s}_{nml} = \sum_{j} w_j d((\vec{r}_l \pm \Delta\vec{r}) - \vec{r}_j) s_m(e_j) \exp(it_j n w) \tag{2.24}$$

Since the moments of the EEDs are already stored, the additional space requirement for storing the harmonic components and the time for computing the same are negligible. These coefficients are then incorporated into the calculation of the rate coefficients in the FKS module. The amplitude and phase of the source function for the n_{th} harmonic for the I_{th} iteration is then obtained from

$$S^{I}_{nml} = [e]_{I-1}, |k_{nml}|, f^{t}_{nml} = \tan^{-1}\frac{\mathrm{Im}(k_{nml})}{\mathrm{Re}(k_{nml})} \tag{2.25}$$

where $[e]_{I-1}$ is the electron density at the end of the previous iteration. To update the rate coefficients accordingly, the effective source function is obtained as the sum of the harmonic components. This is given as

$$S_{ml}(t) = \max\,(0, \sum_{n=0}^{n_{max}} S^{I}_{nml}.N_{m}.\sin(nwt + f_{nml})) \tag{2.26}$$

where n_{max} is the maximum range of harmonics. The source function should, in principle, always be positive. The maximum function is used to account for noise in the EMCS which might result in the sum amplitude of the harmonics being greater than the time average.

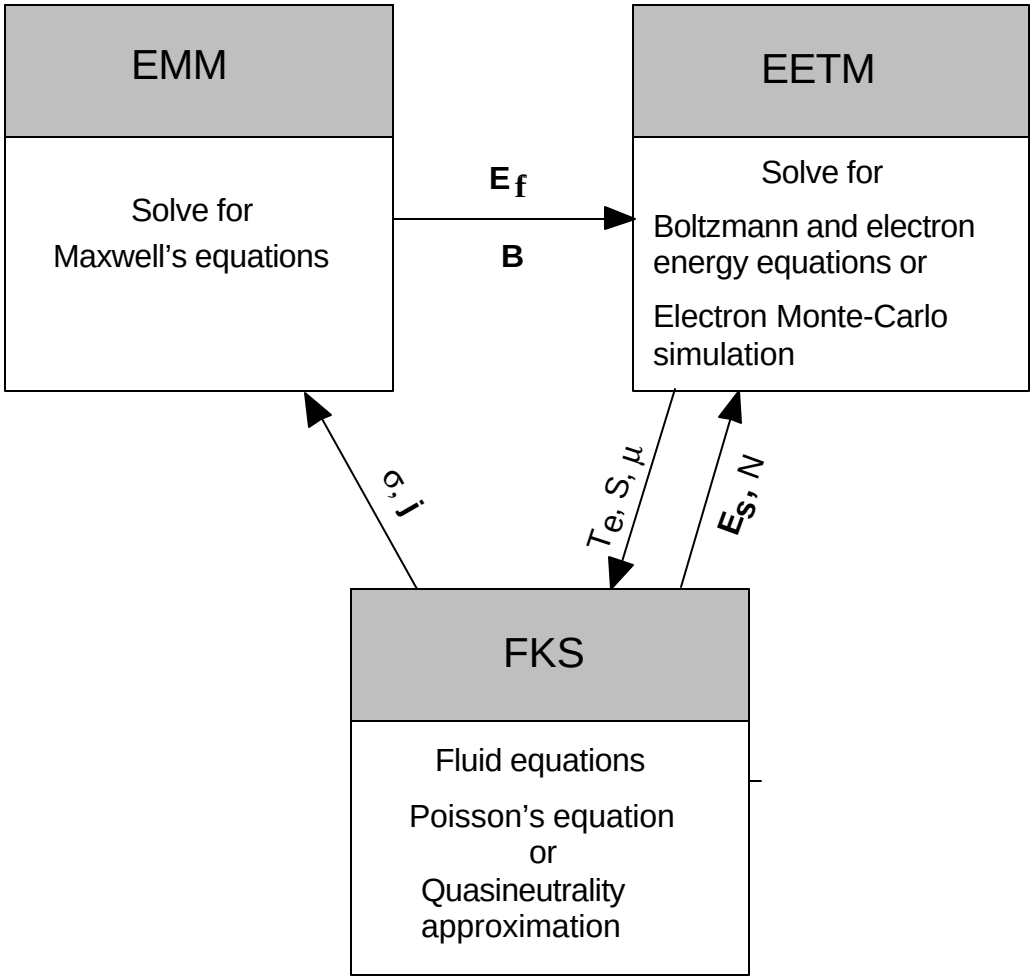

Fig. 2.1. Schematic of the modular HPEM

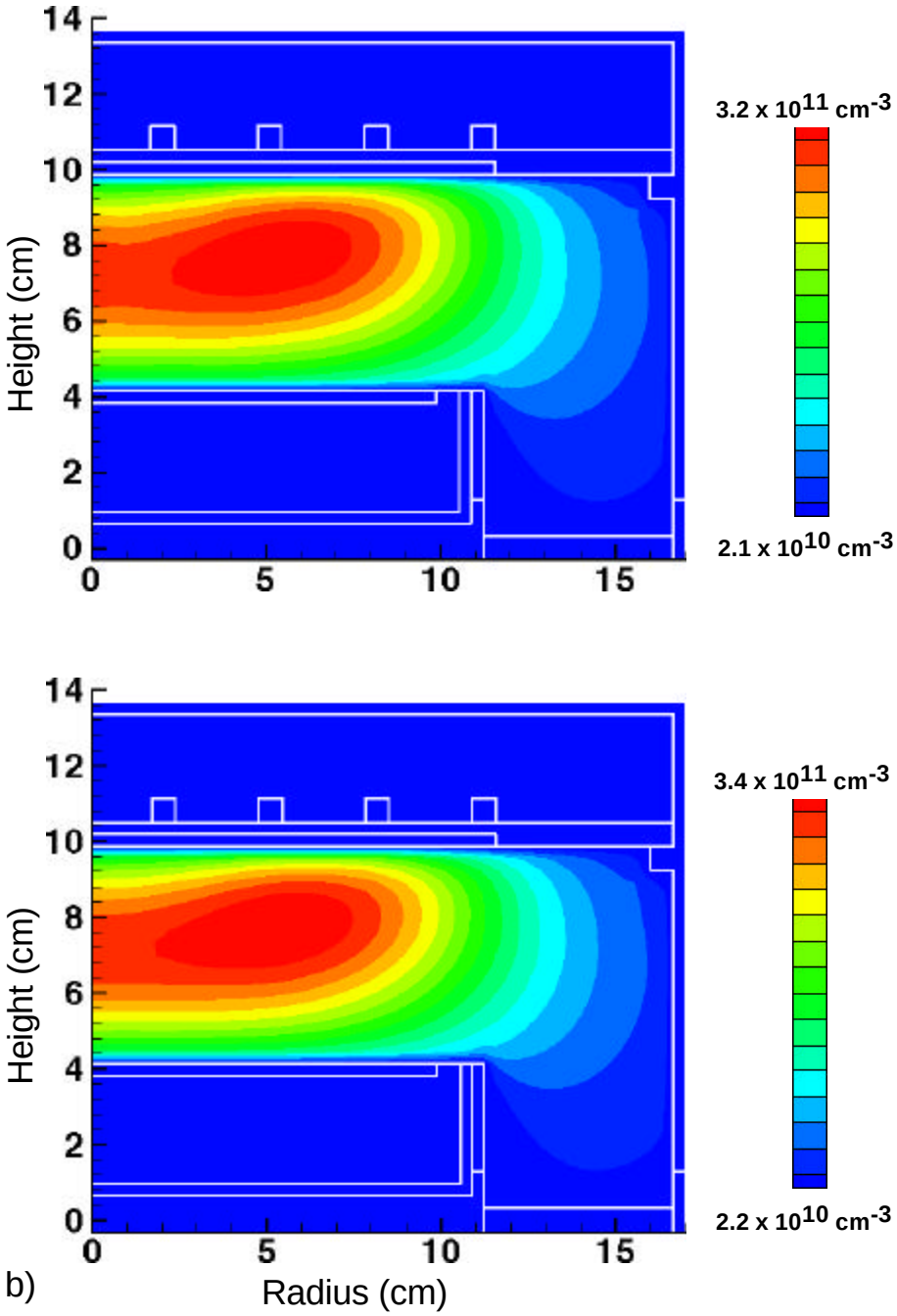

Fig. 2.2. Electron density in an ICP reactor obtained using (a) Conventional MCS method and (b) On-the-Fly Method

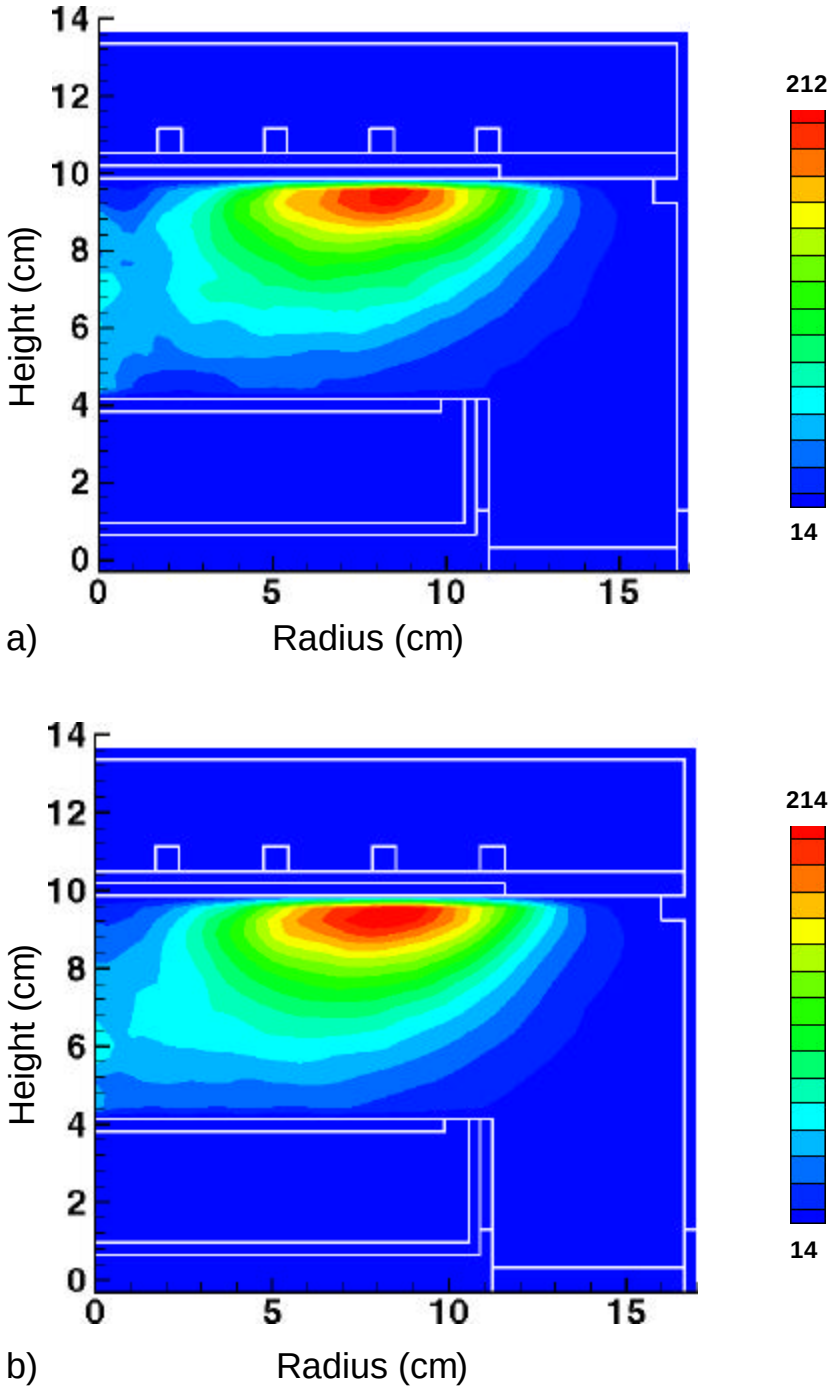

Fig. 2.3. Source functions for electron impact ionization of Argon in an ICP reactor obtained using (a) Conventional MCS method and (b) On-the-Fly Method

2.5 References

[1] P. L. G. Ventzek, R. J. Hoekstra, and M. J. Kushner, J. Vac. Sci. Technol. B **12**, 416 (1993)

[2] P. L. G. Ventzek, M. Grapperhaus, and M. J. Kushner, J. Vac. Sci. Technol. B **16**, 3118 (1994)

[3] W. Z. Collison and M. J. Kushner, Appl. Phys. Lett. **68**, 903 (1996)

[4] M. J. Kushner, W. Z. Collison, M. J. Grapperhaus, J. P. Holland, and M. S. Barnes, J. Appl. Phys. **80**, 1337 (1996)

[5] M. J. Grapperhaus and M. J. Kushner, J. Appl. Phys. **81**, 569 (1997)

[6] S. Rauf and M. J. Kushner, J. Appl. Phys. **81**, 5966 (1997)

[7] F. Y. Huang and M. J. Kushner, J. Appl. Phys. **78**, 5909 (1995).

[8] R. J. Hoekstra and M. J. Kushner, J. Appl. Phys. **79**, 2275 (1996).

[9] H. H. Hwang and M. J. Kushner, Appl. Phys. Lett. **68**, 3716 (1996).

[10] R. J. Hoekstra and M. J. Kushner, J. Vac. Sci. Technol. B **16**, 2102 (1998).

[11] M. E. Riley, *Sandia Report SAND 95-0775. UC-401,* 1995.

3. INVESTIGATIONS OF HARMONIC COMPONENTS OF SOURCE FUNCTIONS IN ARGON/NITROGEN PLASMAS

3.1. Introduction

In this chapter the harmonic components of the source functions are investigated and the results are presented. The simulations are performed for Ar/N_2 gas mixtures. The investigations were performed to quantify the consequences of threshold energy, frequency, pressure and rf magnetic fields on the harmonic components. The variations in the harmonic components for different gas compositions were also investigated.

3.2 Base Case Conditions

The model cell used in all our simulations is shown in Fig. 3.1. The gas mixture was Ar/N_2 with different relative compositions of each component. The rationale for this choice of gases is as follows. Electron impact processes on N_2 are dominated by low threshold reactions and hence are sensitive to the bulk of the EED. Electron impact processes on Ar are dominated by high threshold reactions and hence are sensitive to the tail of the EED. The reaction mechanism of Ar/N_2 plasmas is given in Appendix A.

A base case simulation was performed to provide a point of departure and to determine the electron impact reactions whose harmonic components are most sensitive to the various plasma parameters. The gas pressure was 5 mTorr. The frequency of the rf electric field was 13.56 MHz. Neutral gas temperature in the cell was about 400 K and the gas mixture was Ar/N_2 = 90/10. The power deposition was 650 W. The modules of HPEM were iterated until a quasi-steady state in plasma parameters was obtained. The electron density for the base case is shown in Fig. 3.2. The electron density peaked at about 3.4×10^{11} cm^{-3} at the center of the reactor and

had a low value of about 2.2×10^{10} cm^{-3} in the periphery. The harmonic components of the source functions depend on the modulation of the EEDs. The modulation of the EEDs is in turn dependent on the rf frequency of the electric field and the collision frequency. The tail of the EED is expected to be well modulated, that is, the tail of the EED varies considerably during an rf cycle, whereas the bulk of the EED is relatively constant. This expectation is discussed later in this chapter. With these considerations, two electron impact reactions, which are sensitive to the bulk and tail of the EED, were chosen. The first reaction is the vibrational excitation of N_2 (v=1).

$$e^- + N_2 \rightarrow N_2\ (v=1) + e^-,\ \Delta\varepsilon = 0.29\ eV \qquad (3.1)$$

The threshold energy of this reaction is 0.29 eV. Because the threshold energy is relatively low, this reaction is sensitive to the bulk of the EED and captures the modulation of the bulk of the EED with frequency. This is substantiated using Fig. 3.3. The fraction of electrons above any given threshold energy is shown in Fig. 3.3 for different values of average electron temperature. A Maxwellian electron energy distribution function is integrated for different average electron energies to obtain Fig. 3.3. The base case has an average electron temperature of 3 eV for which the fraction of electrons above the threshold of 0.29 eV $\approx$ 98%. Therefore the vibrational excitation of N_2 tracks the bulk of the EED. The density of the vibrationally excited states of nitrogen is shown in Fig. 3.4. N_2 (V=1) peaked at around 3×10^{11} cm^{-3} at the center of the reactor and had a low value of around 2.5×10^{11} cm^{-3} in the periphery. The second reaction is the electron impact ionization of Ar having a threshold of 16 eV.

$$e^- + Ar \rightarrow Ar^+ + e^- + e^-,\ \Delta\varepsilon = 16\ eV \qquad (3.2)$$

Because the threshold energy of this reaction is relatively high, this reaction is sensitive to the tail of the EED. Its time dependence captures the modulation of the tail of the EED with frequency. For an average electron temperature of 3 eV, around 2% of the electrons have energy greater than 16 eV, and so the rate of this reaction is an indicator of the behavior of the tail of the EED.

3.3 Effect of Threshold Energy

Source functions for the different electron impact reactions were obtained for the base case conditions. Four harmonics were computed. The effective source function is then the sum of both the time-averaged value (the zeroth harmonic) and the higher harmonic components multiplied by their corresponding phases. The effective source function of the electron impact ionization of Ar at different phase values (or different times in the rf cycle) is shown in Fig. 3.5. The effective source function for the vibrational excitation of N_2 is shown in Fig. 3.6. The ratios of the magnitudes of the harmonic components compared to the time-averaged values for both of the reactions are shown in Table. 3.1. At the beginning of the rf cycle, indicated by a phase of zero, the source function for Ar^+ peaks and during the rf cycle it propagates into the reactor. That is the source function decreases near the rf coils and reaches the lowest value at a phase of $\pi/2$. There is considerable modulation in the source function during the rf cycle. The source of Ar^+ is high near the coil and propagates into the cell and the electrons are accelerated into the cell. While the energy gain of the electrons near the coils as obtained from the modulation of the source functions is around 0.75 eV near the coils, it is around 3-4 eV farther away from the coils.

The electron gains momentum and energy as it propagates and hence the modulation of the source function is lower near the coils

The source of N_2 (v=1) is high at the center of the reactor and decreases radially outward towards the gas outlet. In comparison to source functions of electron impact ionization of Ar, the source function for vibrational excitation of N_2 is significantly less modulated. This can be explained as follows. As the average electron temperature increased, there is a considerable increase in the fraction of electrons having energy greater than 16 eV. However as the average electron temperature is increased, there is little increase in the fraction of electrons which have energy greater than 0.29 eV. Also in this case the energy gain of electrons at the center of the reactor is around 0.1eV and decreases to insignificantly lower values at the periphery. Therefore during one rf cycle of the electric field, the quantitative change in the source function of electron impact ionization reaction of Ar is more pronounced and hence the higher modulation in comparison to the vibrational excitation reaction of N_2. The modulation of source functions is larger and more pronounced for higher threshold reactions. To study the effects of the other plasma parameters on the harmonic components of the source functions, only the electron impact ionization of Ar was considered.

3.4 Prominence of the Different Harmonics

The contribution of the different Fourier components to the time dependence of ionization of Ar^+ is discussed in this section. The source function quantifies the production of Ar^+ and so can only be positive. Statistical noise produced by the EMCS might lead to the absolute value of the sum of the different harmonic terms being greater than the time-averaged value and this can cause the source function to become negative during the rf cycle. This is not

physical and so small negative values are ignored. The input is an rf electric field which causes a sinusoidal variation of the electron velocities. However the electron energies which vary as the square of the velocities are positive and hence the electron energies have two positive cycles. Therefore the electron impact source functions which are dependent on the electron temperature have two positive cycles during an rf cycle. Hence the presence of odd harmonics are expected to be negligible. The first harmonic and third harmonic constitute 1.9% and 1.7% of the time-averaged value respectively. This is likely a manifestation of the statistical noise in the EMCS. The modulation of the source function follows the electron temperature and does not imply a sinusoidal variation. Therefore the harmonic content cannot be completely realized by the second harmonic. Hence there is substantial harmonic content in lower even harmonics. The second harmonic constitutes 22.2% of the time-averaged value and the fourth harmonic constitutes 4.9%. The spatial variations of the time-averaged value and the harmonics of the source function of Ar^+ are shown in Fig. 3.7 for the base case. The spatial variations of the time-averaged source function and the even harmonics are similar.

3.5 Effect of Frequency

There is significant harmonic content in the electron impact source functions, which has an important effect on the kinetics of the plasma chemistry. Since the harmonic content is due to the applied voltage, one would expect the frequency of the applied voltage to affect the harmonic content. Electron collision frequency is the number of interactions per second that an electron has with the gas atoms and molecules. Collision frequency is given as

$$\nu_i = \langle N_g \, \sigma \, v \rangle \tag{3.3}$$

where N_g is the gas density, σ is the cross section of the corresponding reaction and v represents the velocity (electron temperature) of the electrons. Ionization cross sections increase with electron energy above threshold and hence the collision frequency increases with increase in the average electron temperature. The variation of the harmonic content with rf frequency is shown in Fig. 3.8. The gas pressure is 5 mTorr, gas mixture Ar/N_2 = 90/10 and power 650 W. The frequency was varied from a few MHz to 50 MHz. The dominant second harmonic decreases as the frequency increases. It constitutes about 20% of the time-averaged value at around 10 MHz and decreases to less than 3% of the time-averaged value at around 30 MHz. A similar trend is seen in the fourth harmonic. The other harmonics do not significantly contribute.

Collision frequencies for ionization reactions estimated from the spatial variations of the source functions at 13.56 MHz are around 8×10^6 s^{-1}. At low frequencies (< 10 MHz) the frequency of the rf field is low compared to the collision frequency of the electrons, $\omega_{rf} << \upsilon_{collision}$. This implies that the number of collisions within a single rf cycle is high. As a result the electrons can respond and come into equilibrium with the electric field. Hence there is significant harmonic content. At higher frequencies (> 10 MHz), the collision frequency is low compared to the frequency of the rf field, $\omega_{rf} >> \upsilon_{collision}$. The electrons undergo many rf cycles between collisions and therefore the effective electric field that the electrons see is the time-averaged value of the electric field. As a consequence, there is little harmonic content at higher frequencies. The first and third harmonics are likely a manifestation of the statistical noise in the EMCS and their frequency variations cannot be qualified.

3.6 Effect of Pressure

The variation of the harmonic components of the source functions, as a function of the pressure, is presented in this section. Since the collision frequency depends on gas density one should expect a pressure dependence on the harmonics of the source functions. The pressure variation of the Fourier components of the source functions is shown in Fig. 3.9 for 13.56 MHz, Ar/N_2 = 90/10, and power 650 W. The gas pressure was varied from a few to 100 mTorr. At higher pressures the local field approximation is valid and the mean free path of the electrons is lower. As a result, the collision frequency of the electrons is higher as compared to the rf field frequency at higher pressures. This can also be understood from the fact that the neutral gas density is directly proportional to the gas pressure and hence when the pressure increases the collision frequency also increases. By arguing in a similar fashion, one can expect the collision frequencies to be low compared to the rf field frequency at lower pressures and hence the harmonic content is expected increase with pressure. This trend is observed for all the harmonics at high pressures ($\geq$ 20 mTorr). However this is not observed at lower pressures for the dominant second harmonic. Although the lower harmonics are due to the statistical noise in the EMCS, when compared to the base case, the lower harmonics constitute a higher harmonic content when more harmonics are generated. This therefore suggests that generation of more harmonics would depict the system better and one can observe the expected trend at lower pressures as well.

3.7 Effect of rf Magnetic Fields

The effect of exclusion of rf magnetic field from the system is presented in this section. Source functions for Ar^+ at different times in an rf cycle in the presence and absence of rf

magnetic fields is shown in Figs. 3.10 and 3.11 for the base case. The electron source function peaks near the coils and propagates into the reactor for both the cases. When the rf magnetic field is included, there is an additional upward force (positive z direction) on the electrons due to the B field. This force as estimated from the source function wave patterns is around 2.5×10^{-16}N. The force due to a magnetic field is given by $\vec{F} = q(\vec{v}\times\vec{B})$. The magnetic field estimated from this equation is around 9.2 G. The magnitude of the rf magnetic field for this case is shown in Fig. 3.12. The magnitude of the rf magnetic field for the base case has a high of 22.1 and low of 2.2. This hence confirms that the spatial variations in the source functions are due to the additional force caused by the rf magnetic field.

However the harmonic content of the source functions cannot be affected by the magnitude of the magnetic fields. Hence in the case where the rf magnetic fields are excluded, the peak values of the source functions are lower than in the case where the rf magnetic field is included.

3.8 Effect of Changes in Gas Mixtures

The effect of different gas compositions on the harmonic content of the source functions is presented in this section. To this end the relative gas compositions of Ar and N_2 were varied in the gas mixture to Ar/N_2 = 80/20 and the simulations were repeated. Only the electron impact ionization of Ar was investigated. The source functions for Ar^+ at different times in the rf cycle for the base case is shown in Fig. 3.13. The spatial variations of the Ar^+ productions is similar to the case where Ar/N_2 = 90/10 and the peak values have a close match too. In both the cases there is a small value for the source function at the center of the reactor which is anomalous. This is due to the statistical noise in the EMCS. This anomalous spatial trend is toned down and

there is smaller Ar^+ production at the center in case of Ar/N_2 = 80/20, indicating lesser statistical noise due to EMCS. The frequency dependencies were studied next and this is shown in Fig. 3.14. The operating conditions of Ar/N_2 = 90/10 were used in this case. The frequency variation showed similar trends to Ar/N_2 = 90/10 and the harmonic content of the various harmonics increased with decreasing frequencies. The percentage of the first and third harmonic with respect to the time-averaged value are 0.5% and 0.4% respectively. This in comparison with 1.9% and 1.7% for Ar/N_2 = 90/10 suggests fewer statistical noises. Pressure dependency of the harmonic content of the source functions was next investigated and this is shown in Fig. 3.15 for frequency 13.56 MHz, power 650 W and pressures of a few mTorr to 100 mTorr. The pressure dependency showed increasing harmonic content with increasing pressure as in Ar/N_2 = 90/10. Trend of increasing harmonic content with pressure is more pronounced for Ar/N_2 = 80/20. The anomalous trend of decreasing harmonic content with pressure at low pressures is also seen with the Ar/N_2 = 80/20 mixture. Including more harmonics in the study can offset this.

3.9 Conclusions

The effects of threshold energy, frequency, pressure, and gas composition on the harmonic content of electron impact source functions were studied. There is considerable harmonic content for higher threshold electron impact processes, as in the electron impact ionization of Ar. The even harmonics had higher amplitude than the odd harmonics, and in particular the second harmonic was dominant. The harmonic content of the source functions was found to decrease with increasing frequency. The harmonic content of the source functions was higher at higher pressures and was more pronounced when the N_2 mole fraction was increased.

Table. 3.1. Harmonic content of the source functions as a fraction of the time-averaged value of the source function for different electron impact reactions.

Ratio of harmonics wrt the time-averaged value	**Electron impact ionization of Ar**	**Vibrational excitation of N_2**
Harmonic 1	0.019	0.007
Harmonic 2	0.222	0.041
Harmonic 3	0.017	0.005
Harmonic 4	0.049	0.008

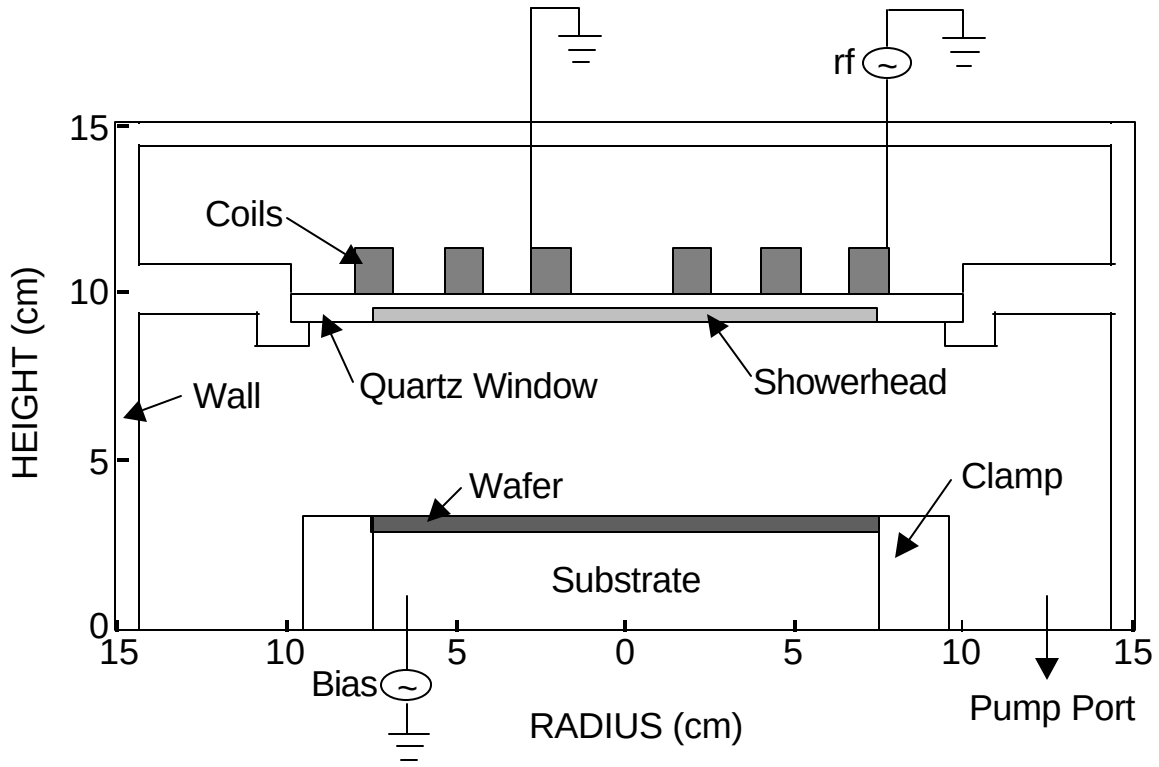

Fig. 3.1. Schematic of the model ICP reactor that was used in all the simulations

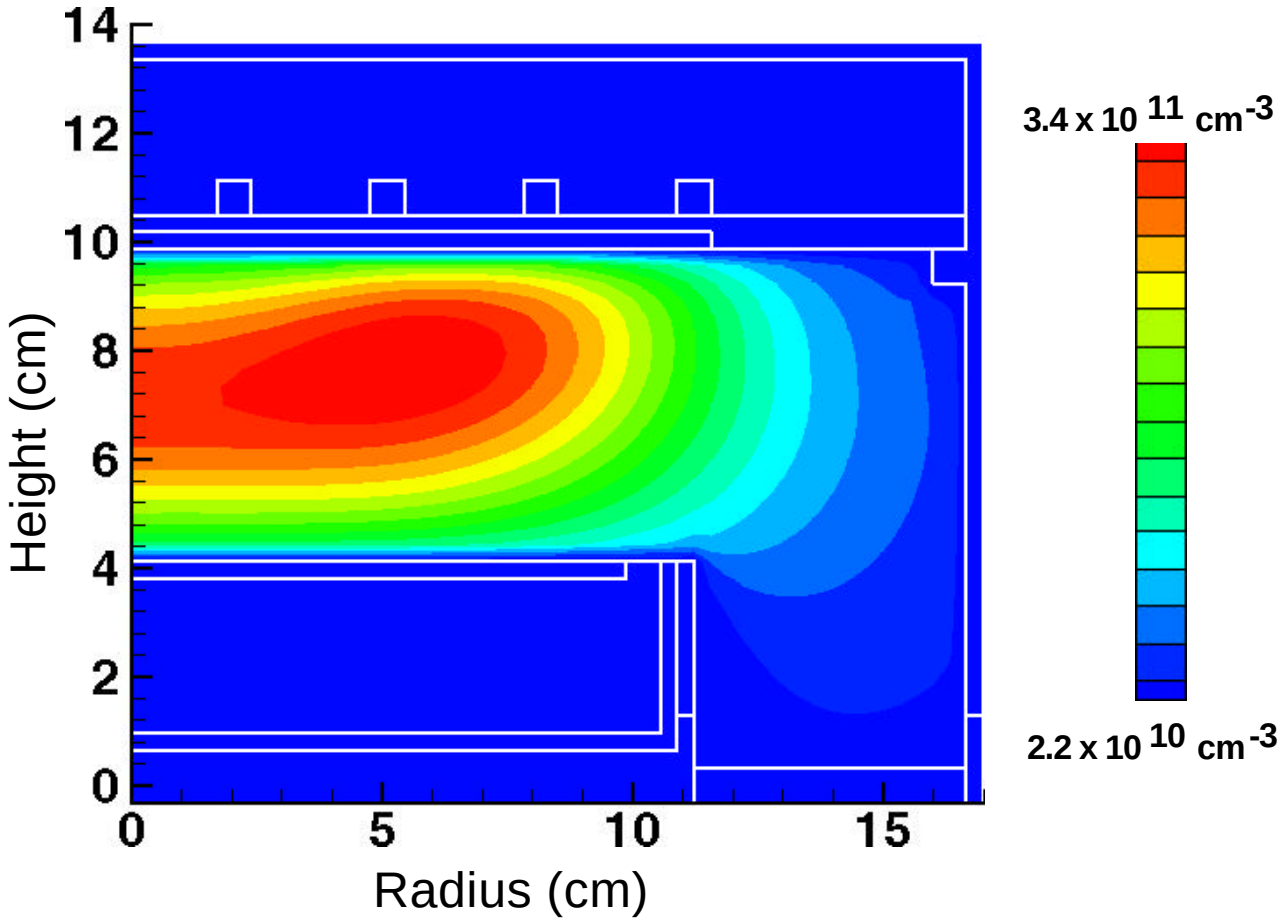

Fig. 3.2. Electron density for the base case

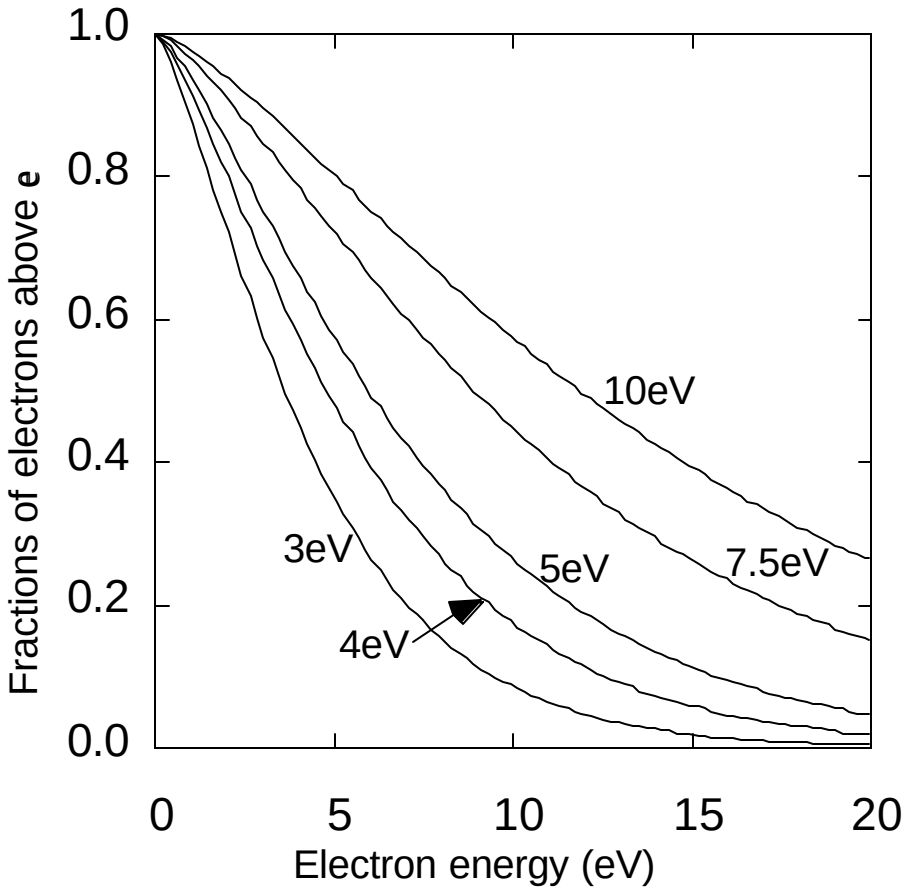

Fig. 3.3. Fraction of electrons above a given threshold energy plotted against energy for electrons with different average electron temperature

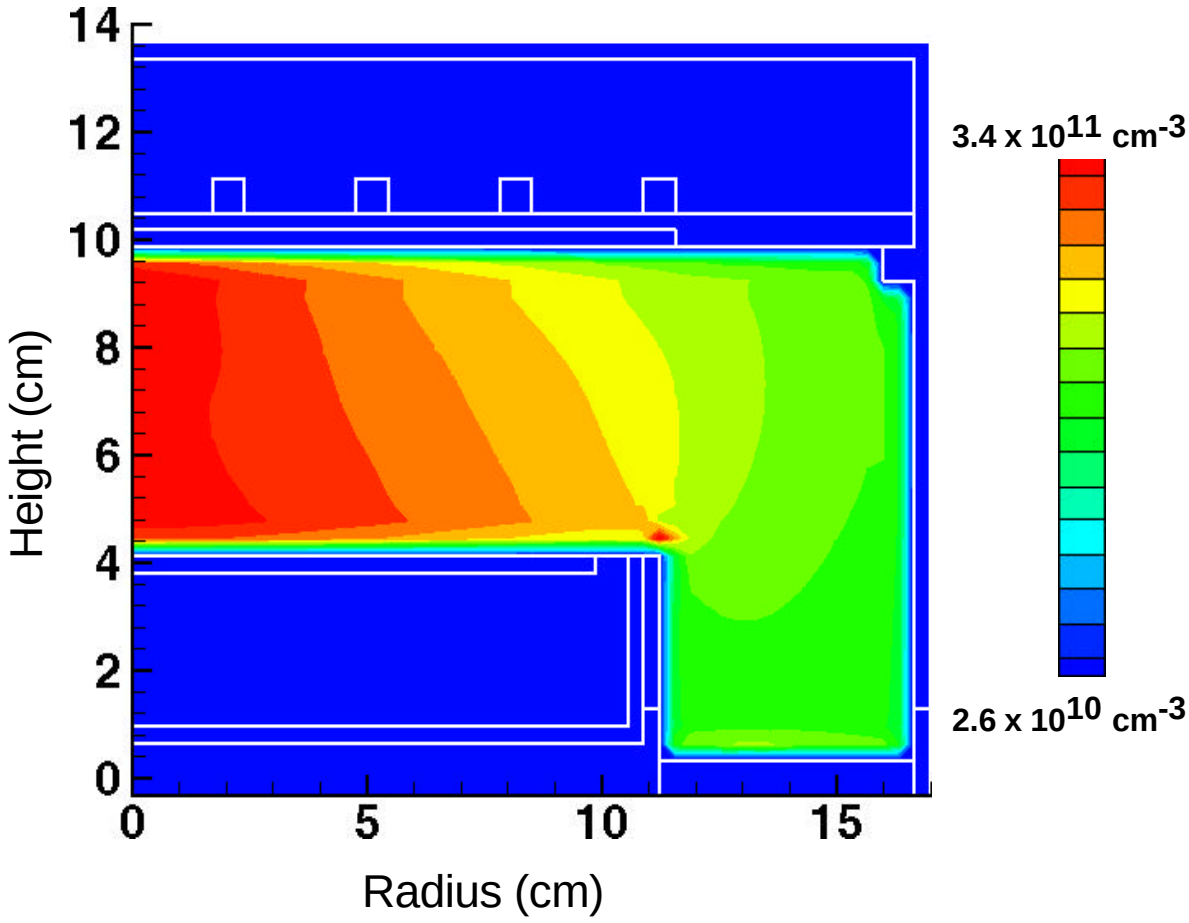

Fig. 3.4. Density of vibrationally excited states of Nitrogen for the base case

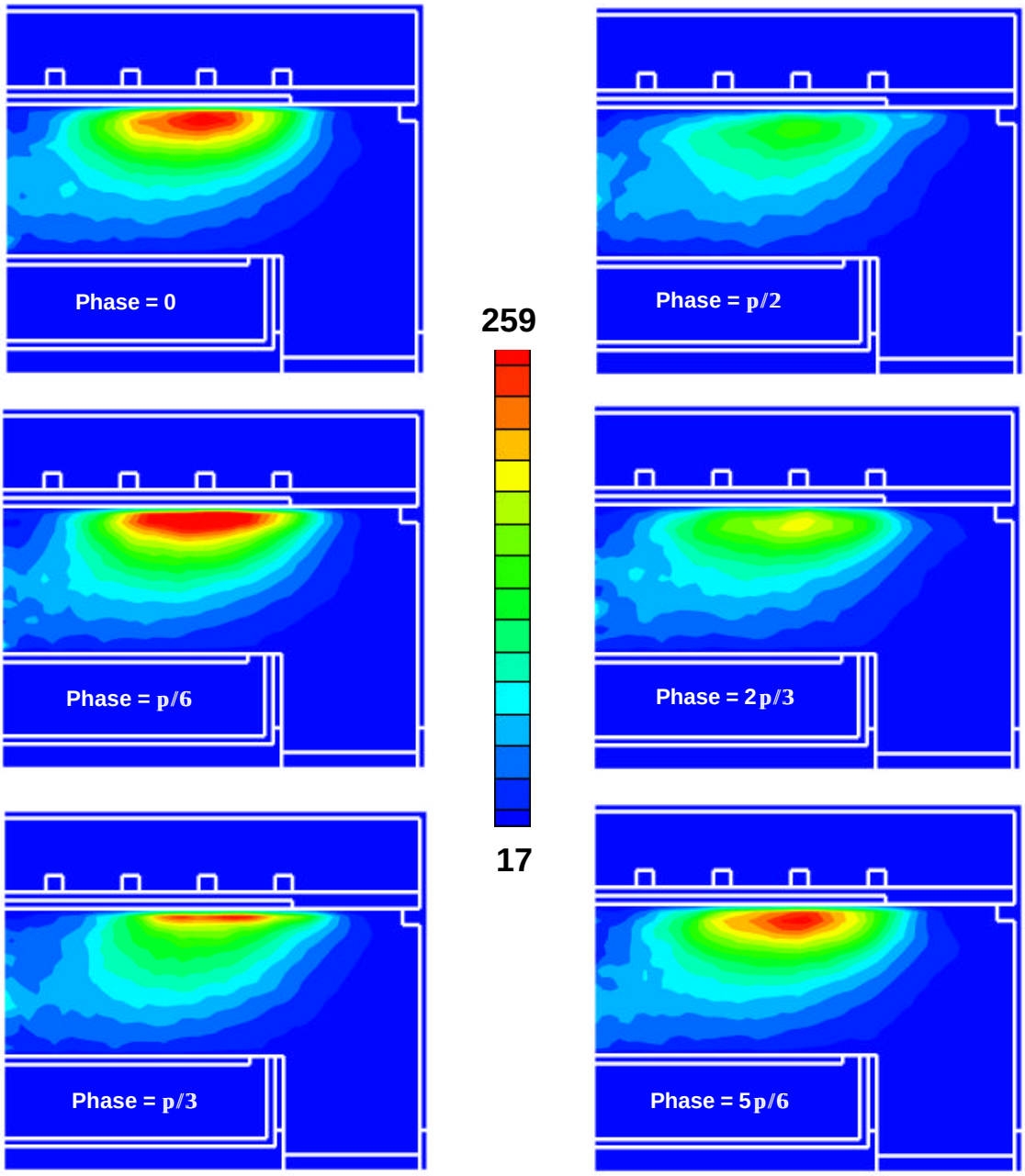

Fig. 3.5. Source functions for electron impact ionization of Argon for the base case conditions at different times during an rf cycle for an Ar/N_2 mixture of 90/10 percent

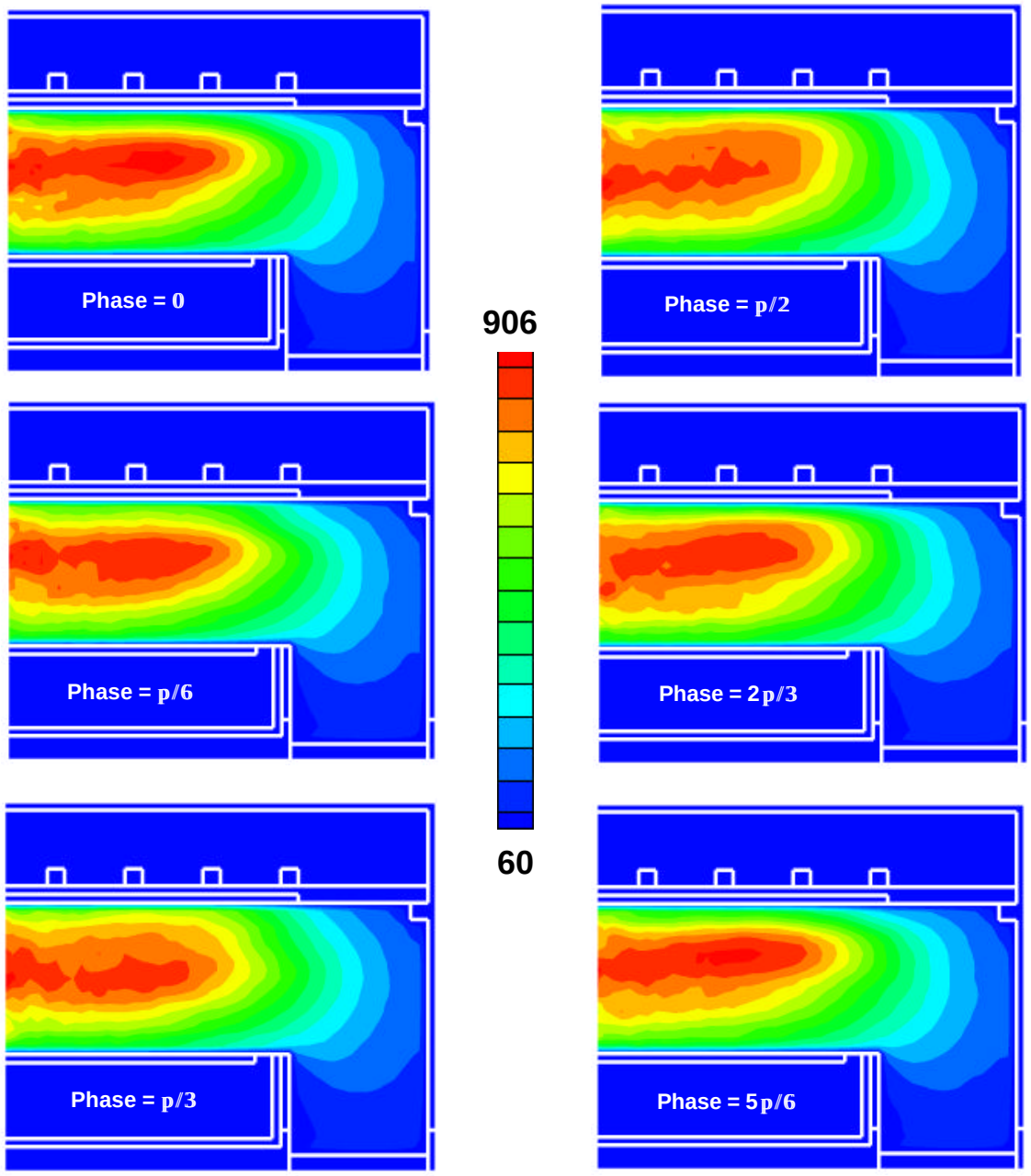

Fig. 3.6. Source functions for vibrational excitation of Nitrogen for the base case conditions at different times during a rf cycle

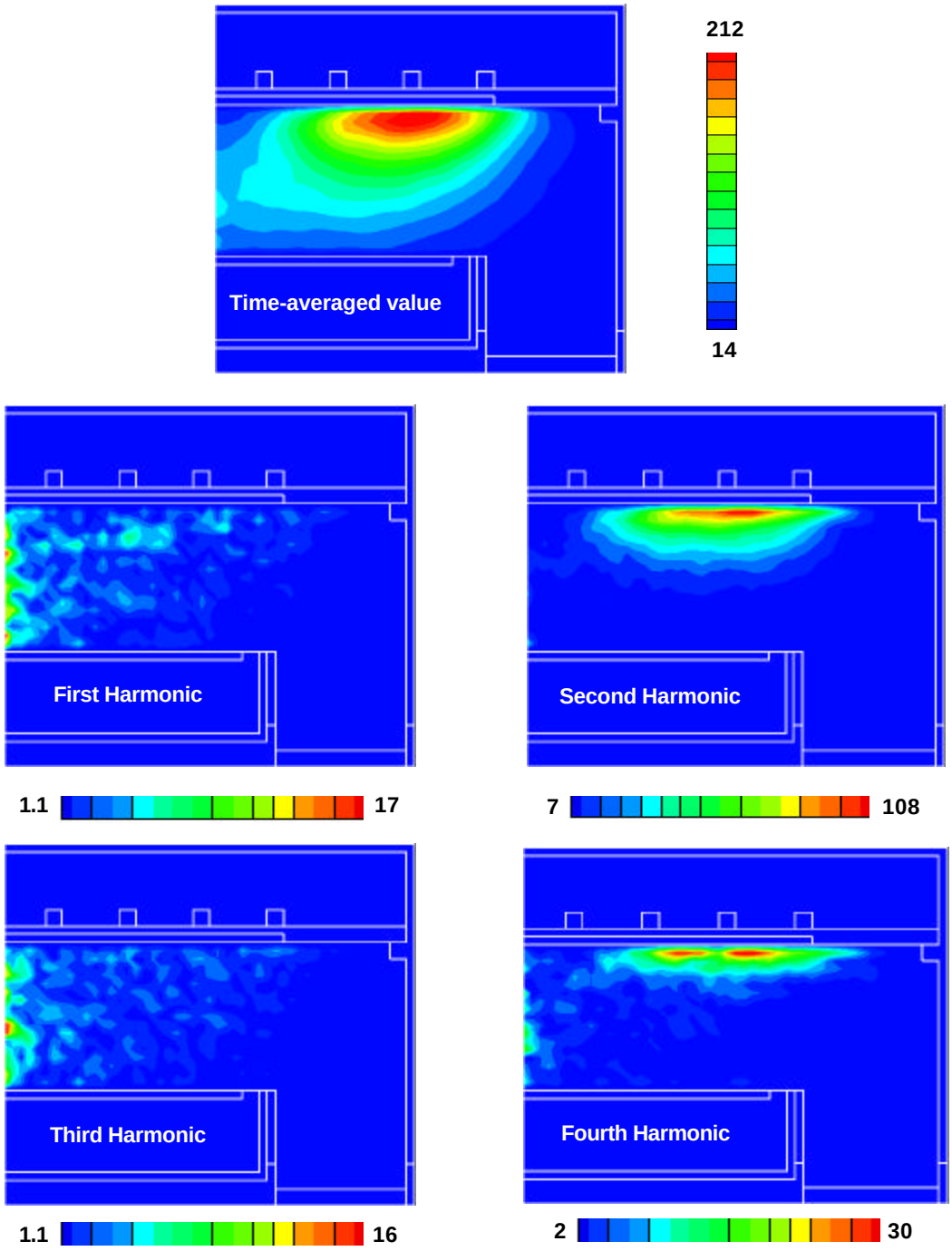

Fig. 3.7. The time-averaged component and the harmonic components of the source functions for electron impact ionization of Argon for the base case conditions

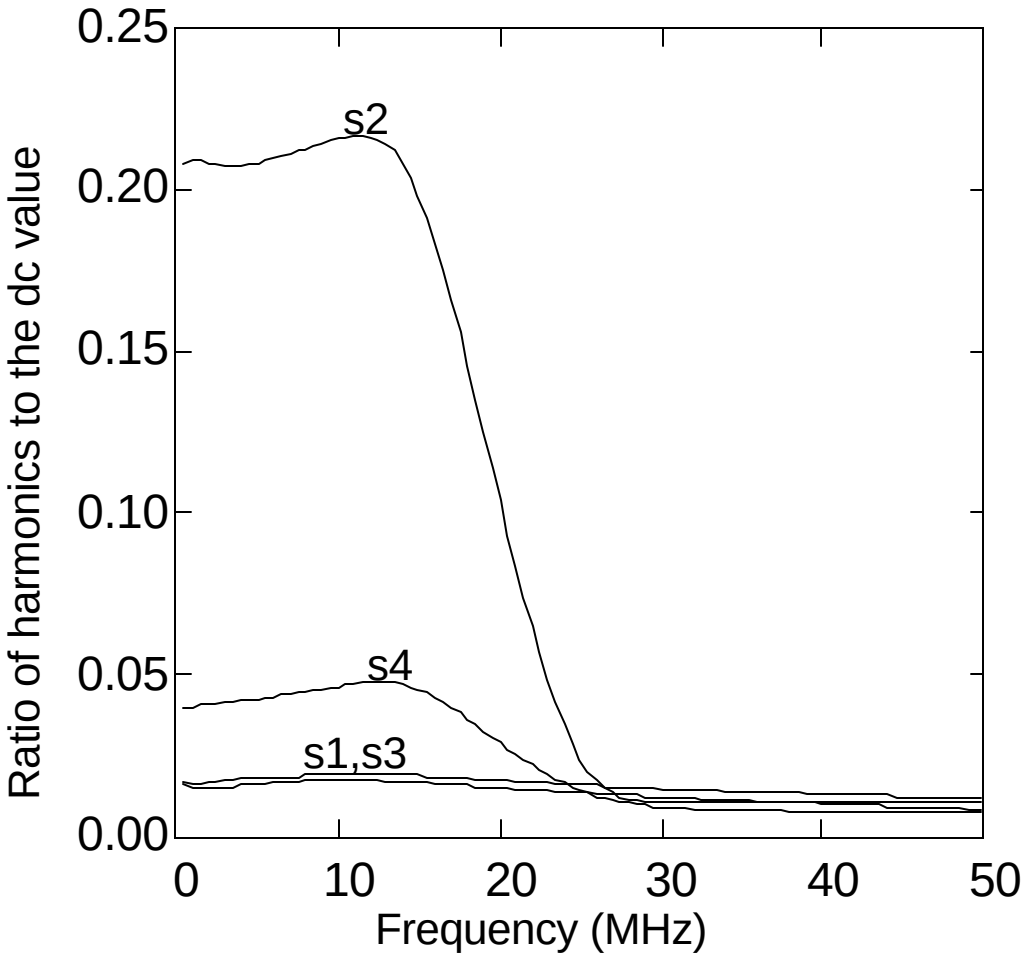

Fig. 3.8. Frequency variation of the harmonic components of the electron impact ionization of Argon for base case conditions and Ar/N_2 90/10

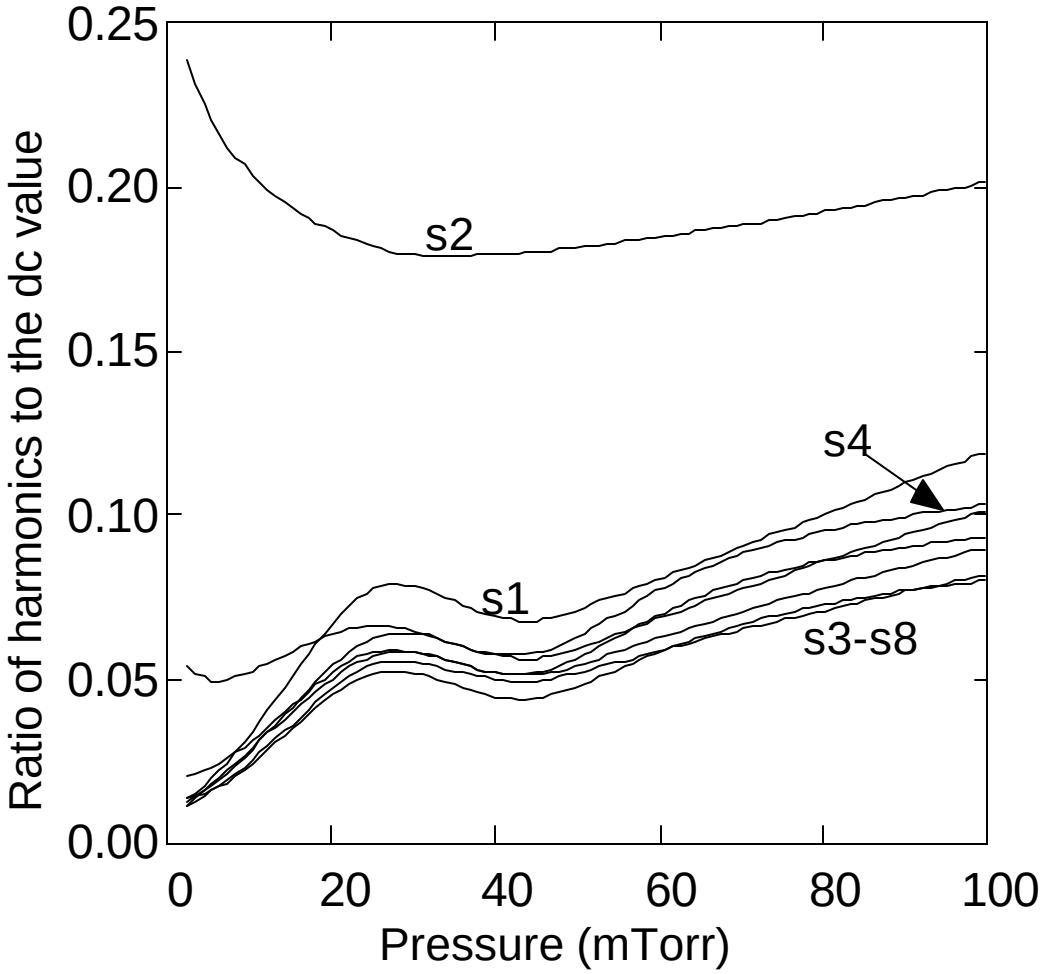

Fig. 3.9. Pressure variation of the harmonic components of the electron impact ionization of Argon for base case conditions and Ar/N_2 90/10

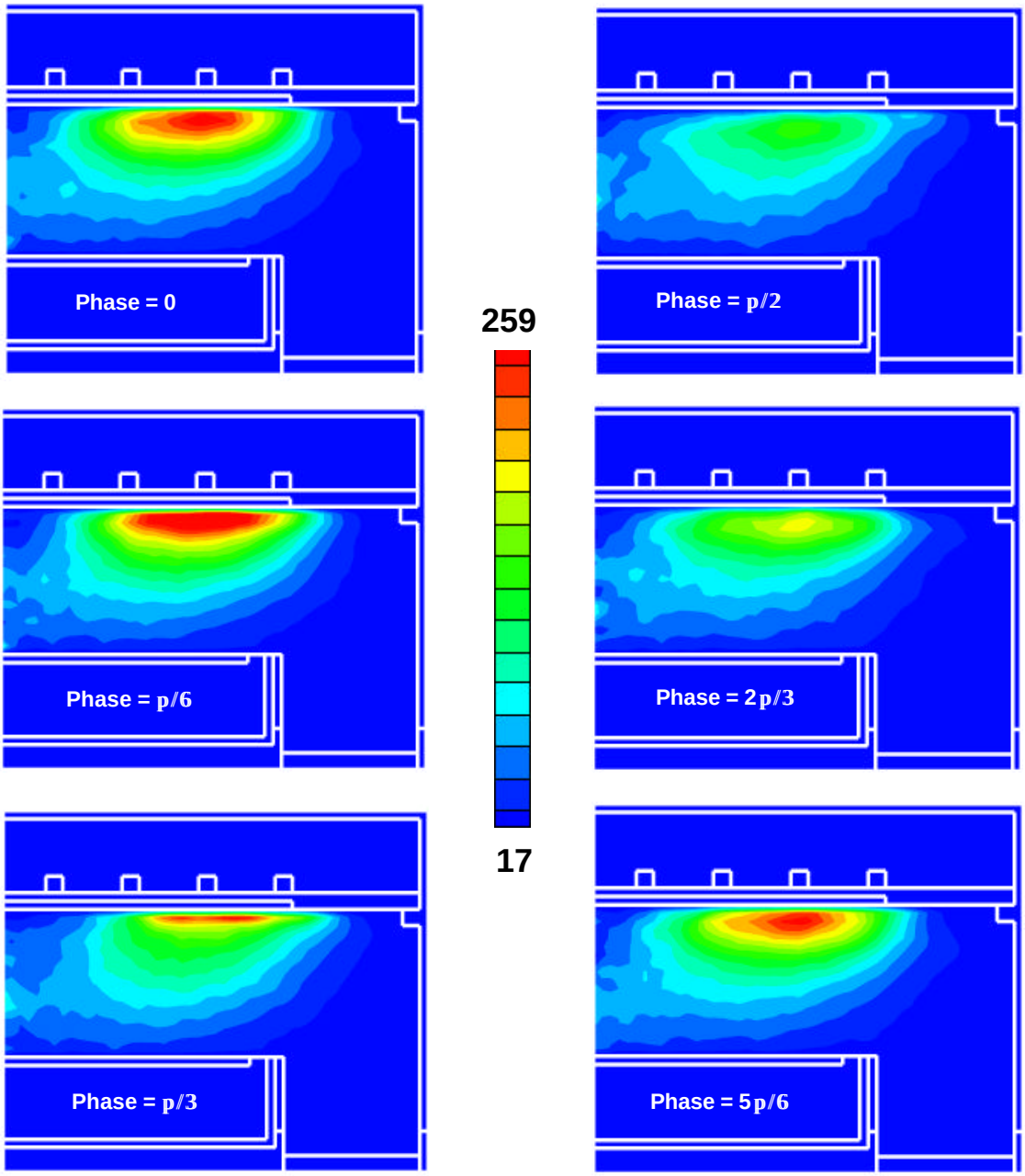

Fig. 3.10. Source functions for electron impact ionization of at different times during a rf cycle in the presence of an rf magnetic field

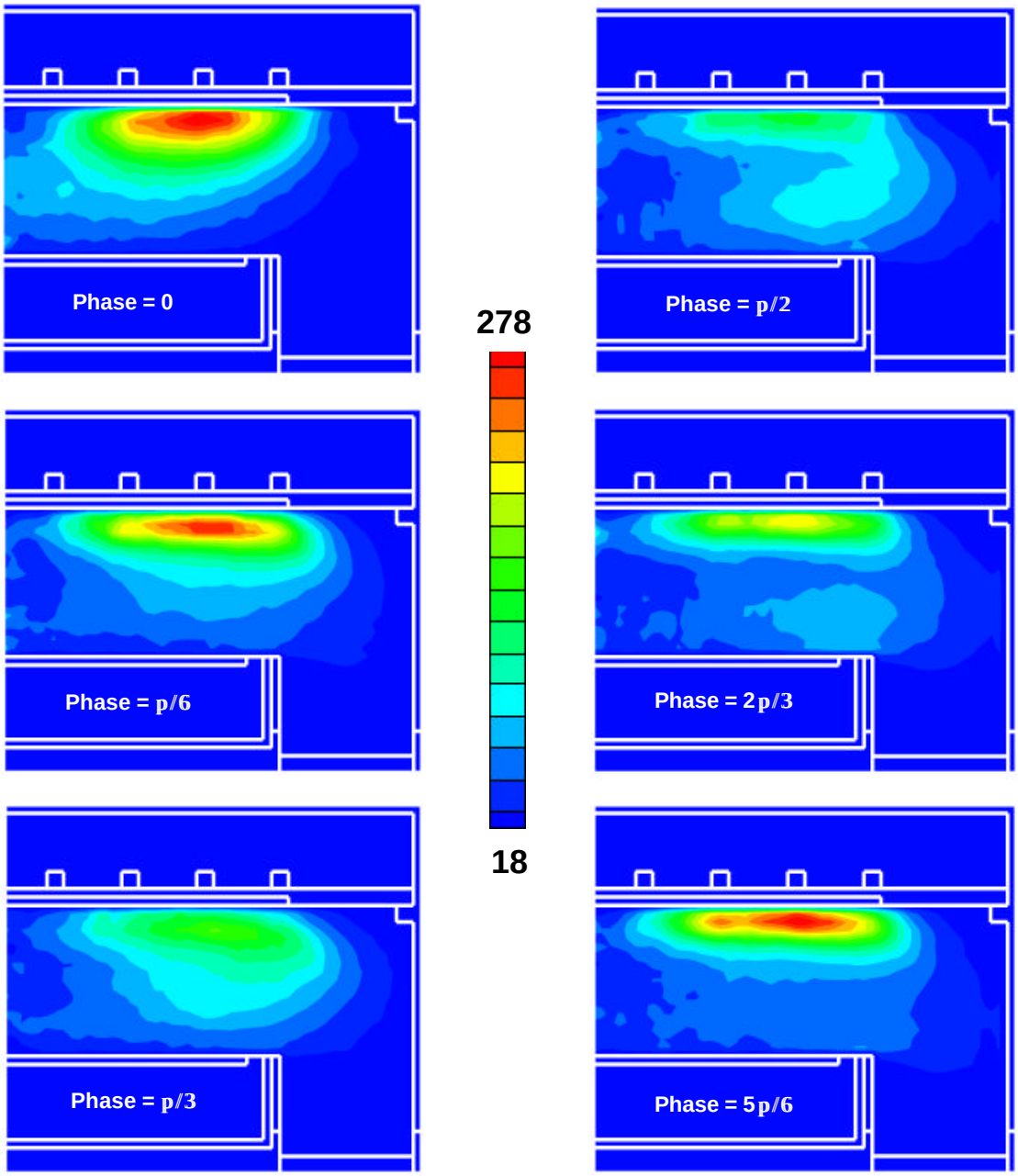

Fig. 3.11. Source functions for electron impact ionization of at different times during an rf cycle in the absence of an rf magnetic field

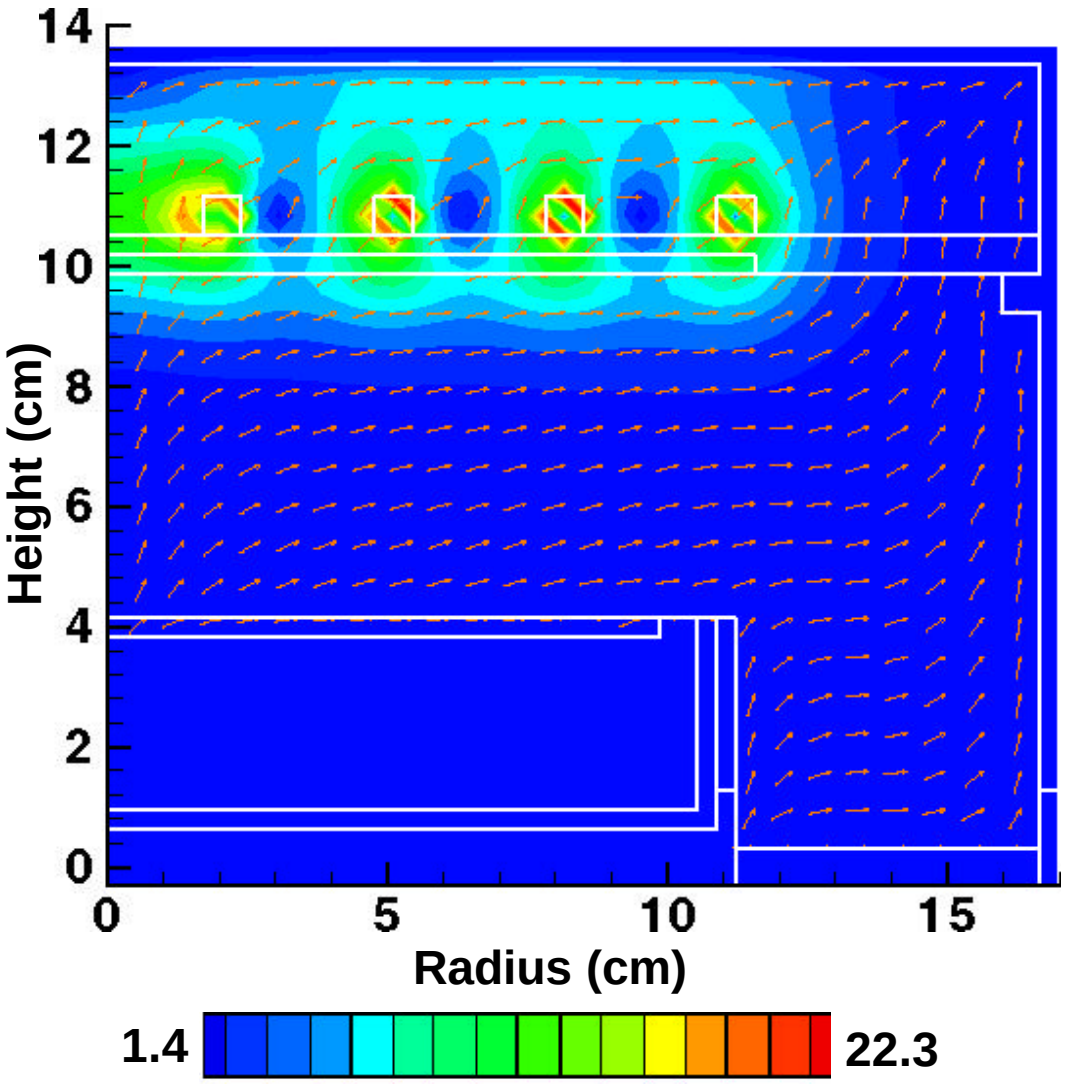

Fig. 3.12. Magnitude of rf B-Field for base case

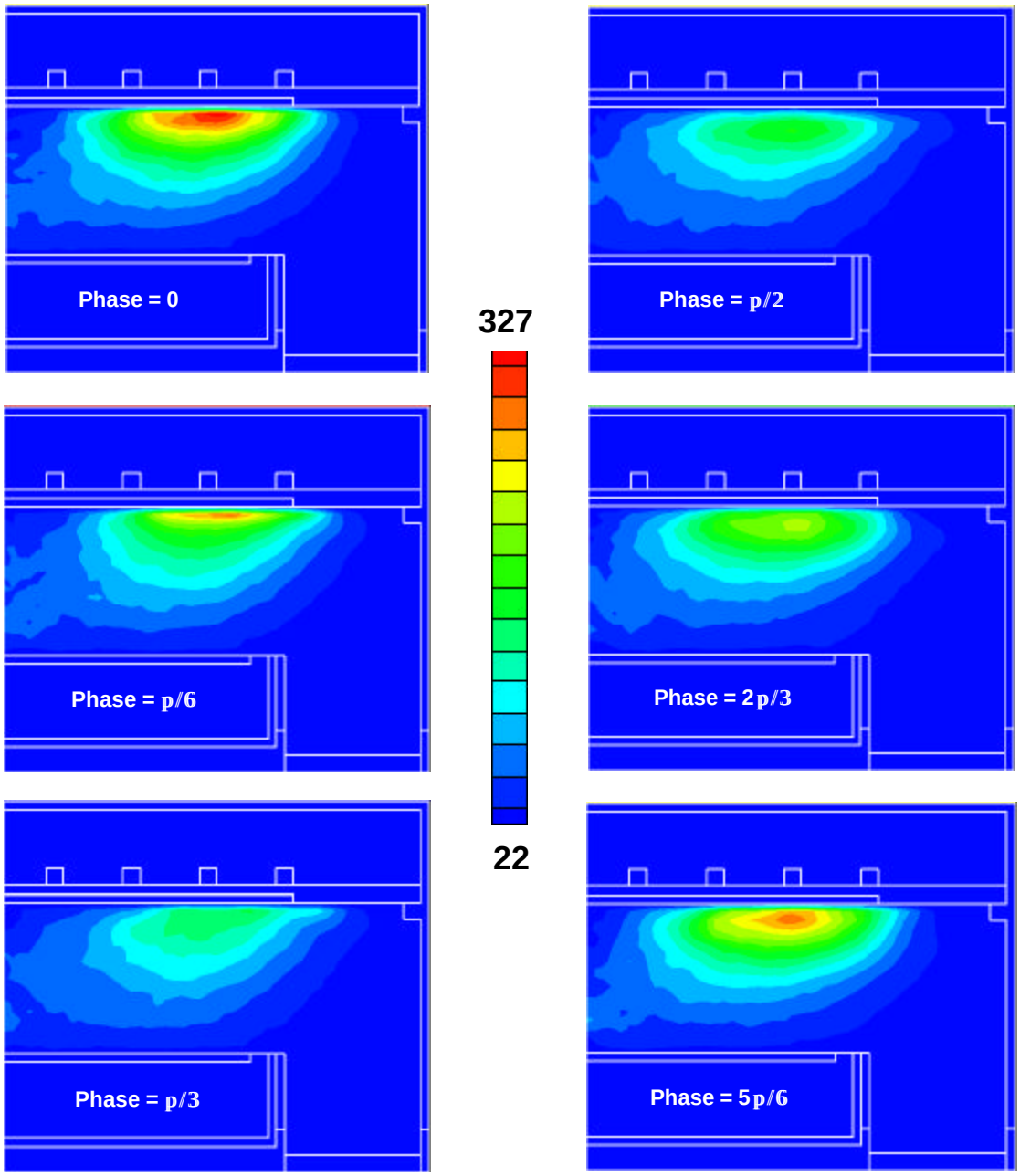

Fig. 3.13. Source functions for electron impact ionization of Argon for the base case conditions at different times during an rf cycle for an Ar/N_2 mixture of 80/20 percent

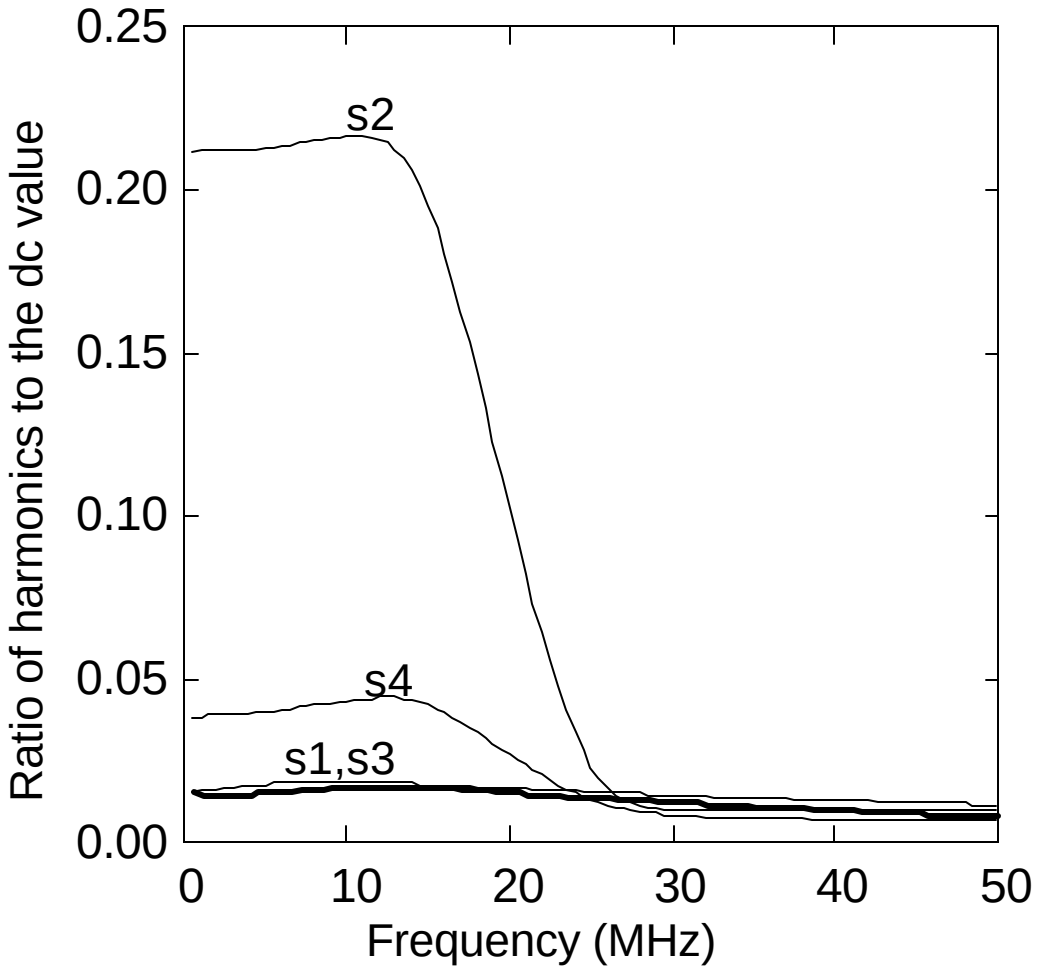

Fig. 3.14. Frequency variation of the harmonic components of the electron impact ionization of Argon for base case conditions and Ar/N_2 80/20

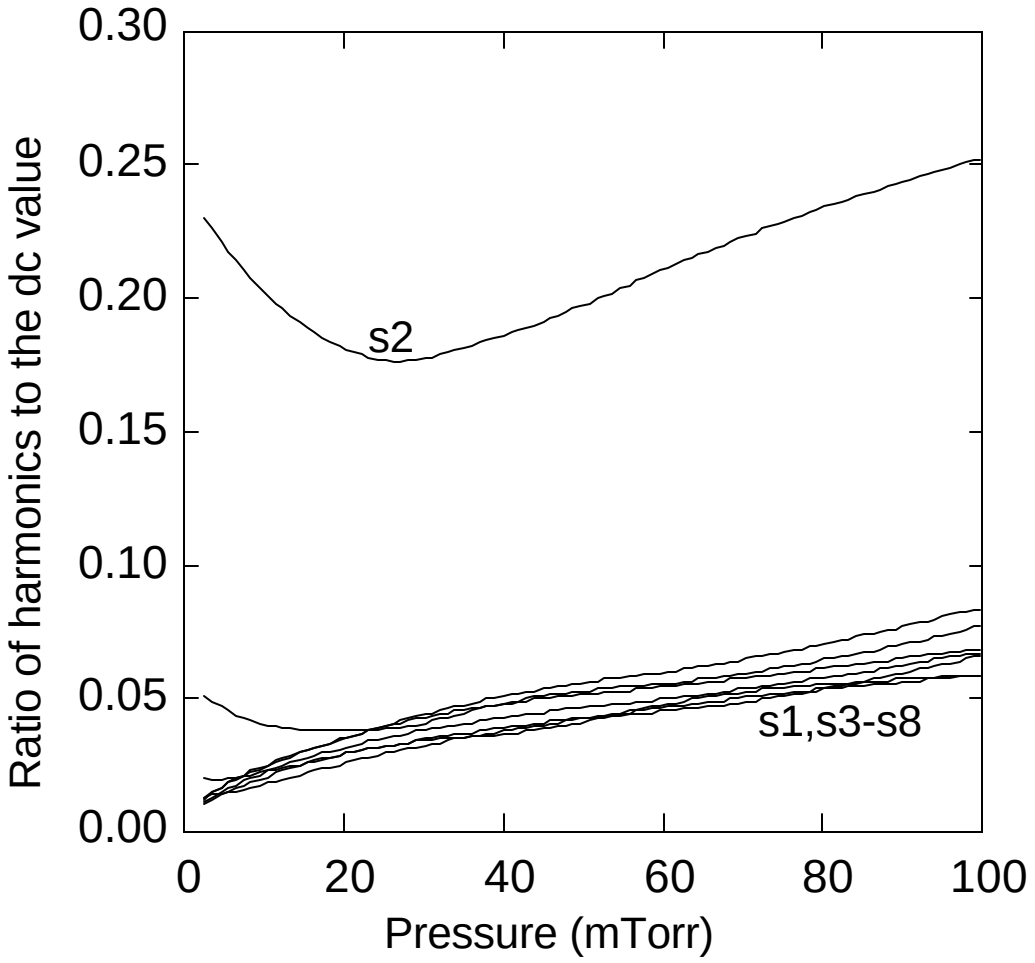

Fig. 3.15. Pressure variation of the harmonic components of the electron impact ionization of Argon for base case conditions and Ar/N_2 80/20

4. CONCLUSIONS

Modeling of plasma processing reactors has been gaining prominence for the last couple of years. The importance and effectiveness of such models depend on their accuracy, which in turn depends on the underlying assumptions about the plasma parameters that characterize them. Of importance are the time-dependent characteristics of electron impact reaction rates and their source functions. Rate coefficients of electron impact reactions and their corresponding source functions are well modulated in an rf electric field, but most plasma processing models use the time-averaged values in depicting the same. Earlier work in this respect has been confined to 1-D models due to the computational complexity involved in modeling this in 2-D.

Present 2-D models often use conventional Monte Carlo techniques for calculating the rate coefficients and source functions. The conventional technique requires calculating and storing the electron energy distribution functions explicitly. This not only poses memory problems but also may be inaccurate due to error in binning. To this end a new 2-D "On-the-fly" Monte Carlo technique was proposed and developed. This method does not explicitly store the EED but only calculates the moments of the distribution functions. The On-the-Fly technique was validated and then extended into computing the time harmonics of the rate coefficients and the source functions of electron impact reactions.

Computational studies were performed for Ar/N_2 gas discharges in an ICP reactor. The harmonic content of the source functions was quantitatively analyzed and its variation with different plasma parameters like threshold energy, frequency of the rf field, gas pressure, rf magnetic fields and gas composition was studied. The tail of the EED was well modulated during the rf period while the bulk of the EED was less modulated. As a result there was

significant harmonic content in the source functions of high threshold processes. The source functions trace the EEDs and vary proportionally with electron energy. Hence there are two positive cycles in the modulation of the source function and as a result the even harmonics dominate.

The effect of rf frequency was studied and the harmonic content decreased with increasing frequency. The effect of gas pressure on the harmonic content was studied. At higher pressures, all the harmonics increased with increasing pressure. However at lower pressures this trend was not observed. Including more harmonics in the investigation could offset this.

The spatial variations of the harmonic content were studied in the absence of the rf magnetic field. In this case, the electron wave propagated further into the reactor. This is because the rf magnetic field exerts an additional upward force on the electrons. The effect on the harmonics of changing the relative compositions in the gas mixture was studied. With increasing N_2 content, the harmonic content of the source functions was more pronounced. However the trends in the variation of the harmonic content with different plasma parameters remained essentially the same.

APPENDIX A: LIST OF REACTIONS FOR Ar/N_2

The reaction chemistry for an Ar/N_2 gas mixture used in the present study is given below:

Electron Impact and Recombination [a]

Reaction	Rate Coefficient [b]	Ref.
$Ar + e \rightarrow Ar^* + e$	c	1
$Ar + e \rightarrow Ar^+ + e + e$	c	1
$Ar^* + e \rightarrow Ar^+ + e + e$	c	1
$Ar^* + Ar^* \rightarrow Ar^+ + e + e$	5×10^{-10}	d
$Ar^* + e \rightarrow Ar + e$	c	1
$Ar^+ + Ar \rightarrow Ar + Ar^+$	5×10^{-10}	d
$e + N_2 \rightarrow N_2(v) + e$	c	2
$e + N_2 \rightarrow N_2^* + e$	c	2
$e + N_2 \rightarrow N_2^+ + e + e$	c	2
$e + N \rightarrow N^* + e$	c	2
$e + N \rightarrow N^+ + e + e$	c	2
$e + N^* \rightarrow N^+ + e + e$	c	2
$e + N_2 \rightarrow N + N + e$	c	2
$e + N_2^* \rightarrow N_2^+ + e + e$	c	2
$e + N_2^+ \rightarrow N^* + N$	c	2
$e + N_2(v) \rightarrow N_2 + e$	c	2
$e + N_2(v) \rightarrow N_2^* + e$	c	2

$e + N_2 (v) \rightarrow N_2^+ + e + e$	c	2
$e + N_2^* \rightarrow N_2 + e$	c	2
$e + N_2^* \rightarrow N_2 (v) + e$	c	2
$e + N^* \rightarrow N + e$	c	2
$Ar^* + N^* \rightarrow N^+ + Ar + e$	5×10^{-10}	d
$Ar^* + N \rightarrow N^* + Ar$	1×10^{-12}	d
$Ar^* + N_2^* \rightarrow N_2^+ + Ar + e$	5×10^{-10}	d
$Ar^* + N_2 \rightarrow N_2 + Ar$	3.6×10^{-11}	d
$Ar^* + N_2 (v) \rightarrow N_2 + Ar$	3.6×10^{-11}	d
$Ar^+ + N_2 \rightarrow N_2^+ + Ar$	1×10^{-11}	d
$Ar^+ + N_2 (v) \rightarrow N_2^+ + Ar$	1×10^{-11}	d
$Ar^+ + N_2^* \rightarrow N_2^+ + Ar$	1×10^{-11}	d
$Ar^+ + N \rightarrow N^+ + Ar$	1×10^{-11}	d
$Ar^+ + N^* \rightarrow N^+ + Ar$	1×10^{-11}	d
$N_2^* + N_2 \rightarrow N_2 + N_2$	1.9×10^{-13}	d
$N_2^* + N \rightarrow N_2 + N$	1×10^{-13}	d
$N_2^* + N^* \rightarrow N_2 + N$	1×10^{-13}	d
$N^* + N_2 \rightarrow N_2 + N$	2×10^{-14}	d
$N^* + N + M \rightarrow N_2^* + M$	2×10^{-32}	d, e

$N + N + M \rightarrow N_2^* + M$	1×10^{-32}	d, e
$N + N + M \rightarrow N_2 + M$	1×10^{-32}	d, e
$N_2^* + N_2^* \rightarrow N_2 + N_2^*$	1.36×10^{-9}	d
$N_2\ (v) + N_2 \rightarrow N_2 + N_2$	1×10^{-13}	d
$N_2\ (v) + N \rightarrow N_2 + N$	1×10^{-14}	d
$N_2\ (v) + N^* \rightarrow N_2 + N$	1×10^{-14}	d
$N_2^+ + N \rightarrow N^+ + N_2$	5×10^{-12}	d
$N_2^+ + N^* \rightarrow N^+ + N_2$	1×10^{-10}	d
$N^+ + N \rightarrow N^+ + N$	5×10^{-10}	d
$N_2^+ + N_2 \rightarrow N_2^+ + N_2$	5×10^{-10}	d
$N_2\ (v) + Ar \rightarrow N_2 + Ar$	1×10^{-14}	d

[a] Only reactions directly affecting species densities are shown here. Additional electron impact collisions (e.g., momentum transfer, vibrational excitation) are included in the EETM.

[b] Rate coefficients have units cm^3s^{-1} unless noted otherwise.

[c] Computed using the electron energy distribution and electron impact cross section from cited reference.

[d] Estimated.

[e] Refers to rate units of cm^6s^{-1}

References

[1] M. Hayashi, Nagoya Institute of Technology Report No. IPPJ-AM-19, 1991.

[2] Y. Itikawa, M. Hayashi, A. Ichimura, K. Onda, K. Sakimoto, K. Takayanagi, M. Nakamura, H. Nishimura, and T. Takayanagi, J. Phys. Chem. Ref. Data Reprint Number 299, **15** (3), 985 (1986).